A&A 474, 393–407 (2007)
DOI: 10.1051/0004-6361:20078021

Astronomy & Astrophysics

Excitation mechanisms in newly discovered H_2-bearing damped Lyman-α clouds: systems with low molecular fractions⋆,⋆⋆

P. Noterdaeme[1], C. Ledoux[1], P. Petitjean[2,3], F. Le Petit[4], R. Srianand[5], and A. Smette[1]

[1] European Southern Observatory, Alonso de Córdova 3107, Casilla 19001, Vitacura, Santiago, Chile
e-mail: pnoterda@eso.org
[2] Institut d'Astrophysique de Paris, CNRS – Université Pierre et Marie Curie, 98bis Boulevard Arago, 75014 Paris, France
[3] LERMA, Observatoire de Paris, 61 Avenue de l'Observatoire, 75014 Paris, France
[4] LUTH, Observatoire de Paris, 61 Avenue de l'Observatoire, 75014 Paris, France
[5] IUCAA, Post Bag 4, Ganesh Khind, Pune 411 007, India

Received 5 June 2007 / Accepted 20 July 2007

ABSTRACT

Aims. We probe the physical conditions in high-redshift damped Lyman-α systems (DLAs) using the observed molecular fraction and the rotational excitation of molecular hydrogen.
Methods. We search for Lyman- and Werner-band absorption lines of molecular hydrogen in the VLT/UVES spectra of background QSOs at the redshift of known DLAs.
Results. We report two new detections of molecular hydrogen in the systems at $z_{\rm abs} = 2.402$ and 1.989 toward, respectively, HE 0027−1836 and HE 2318−1107, discovered in the course of the Hamburg-ESO DLA survey. We also present a detailed analysis of our recent H_2 detection toward Q 2343+125. All three systems have low molecular fractions, $\log f \leq -4$, with $f = 2N(H_2)/(2N(H_2) + N(\mathrm{H\,I}))$. Only one such H_2 system was known previously. Two of them (toward Q 2343+125 and HE 2318−1107) have high-metallicities, [X/H] > -1, whereas the DLA toward HE 0027−1836 is the system with the lowest metallicity ([Zn/H] $= -1.63$) among known H_2-bearing DLAs. The depletion patterns for Si, S, Ti, Cr, Mn, Fe and Ni in the three systems are found to be very similar to what is observed in diffuse gas of the Galactic halo. Molecular hydrogen absorption from rotational levels up to $J = 5$ is observed in a single well-defined component toward HE 0027−1836. We show that the width (Doppler parameter) of the H_2 lines increases with increasing J and that the kinetic energy derived from the Doppler parameter is linearly dependent on the relative energy of the rotational levels. There is however no velocity shift between lines from different rotational levels. The excitation temperature is found to be 90 K for $J = 0$ to $J = 2$ and ∼500 K for higher J levels. Single isothermal PDR models fail to reproduce the observed rotational excitations. A two-component model is needed: one component of low density (∼50 cm^{-3}) with weak illumination ($\chi = 1$) to explain the $J \leq 2$ rotational levels and another of high density (∼500 cm^{-3}) with strong illumination ($\chi = 30$) for $J \geq 3$ levels. However, the juxtaposition of these two PDR components may be ad-hoc and the multicomponent structure could result either from turbulent dissipation or C-shocks.

Key words. galaxies: ISM – galaxies: quasars: absorption lines – quasars: individual: HE 0027-1836 – quasars: individual: HE 2318-1107 – quasars: individual: Q 2343+125

1. Introduction

High-redshift damped Lyman-α systems (DLAs) are the absorbers of highest H I[1] column density seen in QSO spectra, with $N(\mathrm{H\,I}) \geq 2 \times 10^{20}$ cm^{-2}. These absorbers are a major reservoir of neutral hydrogen at $2 \leq z \leq 3$ (e.g. Prochaska et al. 2005) and have long been identified as the precursors of present day galaxies (see Wolfe et al. 2005, for a recent review). Our understanding of DLAs is primarily based on absorption-line studies, involving the detection of low-ionization metal transitions and, in a few cases, molecular hydrogen (e.g. Ledoux et al. 2003; Srianand et al. 2005). Molecular hydrogen is conspicuous in our Galaxy: lines of sight with $\log N(\mathrm{H\,I}) \geq 21$ usually have $\log N(H_2) \geq 19$ (Savage et al. 1977; Rachford et al. 2002) whilst high-redshift ($z_{\rm abs} > 1.8$) H_2-bearing DLAs are rare with only ten detections reported up to now, with redshifts up to $z_{\rm abs} = 4.2$ (Ledoux et al. 2006). Petitjean et al. (2006) noted a correlation between the presence of molecular hydrogen and the metallicity ([X/H] $= \log N(\mathrm{X})/N(\mathrm{H}) - \log \mathrm{X/H}_\odot$, with X = Zn, S or Si) in the gas that may help select the best candidates for future surveys. Indeed, 40% of the [X/H] > -1.3 DLAs have $\log f > -4$, with $f = 2N(H_2)/(2N(H_2) + N(\mathrm{H\,I}))$. On the other hand, only 15% of the overall sample (with $-2.5 <$ [X/H] < -0.3) have $\log f > -4$. Furthermore, up to now, there is no H_2 detection in [X/H] < -1.5 DLAs, down to a detection limit of typically $N(H_2) = 2 \times 10^{14}$ cm^{-2}.

The distribution of molecular fractions is observed to be bimodal: all the upper limits are lower than $\log f = -4.5$, whereas all detections above this limit have $\log f > -3$. Low molecular fractions (with $\log f \leq -4$) are basically unexplored (see

⋆ Based on observations carried out at the European Southern Observatory (ESO) under progs. ID 67.A-0022, 69.A-0204, 072.A-0346, 072.A-0442, 073.A-0071 and 074.A-0201 with the UVES spectrograph installed at the Very Large Telescope (VLT) Kueyen UT2 on Cerro Paranal, Chile.

⋆⋆ Figures 19–25 are only available in electronic form at http://www.aanda.org

[1] To avoid confusion, we use the convenient spectroscopic notation (e.g. Si II for Si$^+$) for atoms and ions following the convention widely used in this field.

however Levshakov et al. 2002). Up to now, only two low-f systems have been reported, in the DLA at $z_{abs} = 3.025$ toward Q 0347−383 ($\log f = -5.9$; Levshakov et al. 2002; Ledoux et al. 2003) and in the DLA at $z_{abs} = 2.431$ toward Q 2343+125 ($\log f = -6.4$; Petitjean et al. 2006).

Molecular hydrogen is primarily formed on the surface of dust grains in the interstellar medium (e.g. Hollenbach & Salpeter 1971), but can also result from the formation of negative hydrogen (H^-) if the gas is warm and dust-free (e.g. Black et al. 1987). H_2 is also formed in the gas phase by radiative association of H^+ with H to form H_2^+, followed by charge transfer with H. However, the reaction is slow in the conditions prevailing in the DLA gas. Spitzer & Jenkins (1975) first showed that the observed relative populations of the H_2 rotational levels cannot be described by a single excitation temperature. Whilst the low-J levels can be thermalised, the high-J levels are populated by direct formation on these levels and UV pumping (e.g. Jura 1975) or by collisions if part of the gas is heated to temperatures above a few hundred K by, for example, turbulent dissipation and/or shocks (e.g. Joulain et al. 1998; Cecchi-Pestellini et al. 2005). In DLAs, H_2 excitation is generally explained by predominant UV pumping (Hirashita & Ferrara 2005).

Here we present the analysis of H_2 absorptions in three DLAs, at $z_{abs} = 2.431$, 1.989, and 2.402 toward, respectively, Q 2343+125, HE 2318−1107, and HE 0027−1836. The three systems have low molecular fractions according to the above criterion, $\log f \leq -4$. The $z_{abs} = 2.431$ system toward Q 2343+125 has the lowest molecular fraction measured till now in a DLA. We recently reported this detection as part of a high-metallicity ([X/H] > −1.3) UVES DLA sample (Petitjean et al. 2006). A detailed analysis of the system is given here. The latter two systems are new detections discovered during the Hamburg-ESO DLA survey (Smette et al. 2005, Smette et al. 2007, in prep.) and are reported for the first time. H_2 is detected in rotational levels up to $J = 5$ in the DLA toward HE 0027−1836. This is the system with the lowest metallicity amongst known H_2-bearing DLAs. We present the observations in Sect. 2 and properties of the three systems toward respectively Q 2343+125, HE 2318−1107 and HE 0027−1836 in Sects. 3 to 5. We discuss the H_2 excitation toward HE 0027−1836 in Sect. 6 and comment on metallicity and depletion in Sect. 7. We conclude in Sect. 8.

2. Observations

The quasars Q 2343+125, HE 2318−1107, and HE 0027−1836 were observed in visitor mode with the Ultraviolet and Visible Echelle Spectrograph (UVES, Dekker et al. 2000) mounted on the ESO Kueyen VLT-UT2 8.2 m telescope on Cerro Paranal in Chile. Q 2343+125 was observed on October 29, 2003 under program ID. 072.A-0346. HE 2318−1107 and HE 0027−1836 were observed on September 16, 17, and 18, 2004, under program ID. 073.A-0071. HE 0027−1836 was re-observed on October 8 and 9, 2004, under program ID. 074.A-0201. Observations were supplemented with UVES data from the ESO archive, progs. 67.A-0022 and 69.A-0204 (P.I: D'Odorico) for Q 2343+125 and prog. 072.A-0442 (P.I: Lopez) for HE 2318−1107 and HE 0027−1836. The data were reduced using the UVES pipeline (Ballester et al. 2000) which is available as a context of the ESO MIDAS data reduction system. The main characteristics of the pipeline are to perform a precise inter-order background subtraction, especially for master flat-fields, and to allow for an optimal extraction of the object signal rejecting cosmic rays and performing sky subtraction at the same time. The pipeline products were checked step by step. The wavelength scale of the reduced spectrum was then converted to vacuum-heliocentric values and the portions of the spectrum corresponding to different settings were each rebinned to a constant wavelength step. No further rebinning was performed during the analysis of the whole spectrum. Individual 1-D exposures were scaled, weighted and combined together. Standard Voigt-profile fitting methods were used for the analysis to determine column densities using the vacuum wavelengths and oscillator strengths from Morton (2003) for metal ions, except for the oscillator strengths of Fe II $\lambda\lambda\lambda\lambda$1063,1064,1112,1121 (Howk et al. 2000) and Ni II $\lambda\lambda$1317,1370 (Jenkins & Tripp 2006), and the wavelengths of S II $\lambda\lambda$1250,1253 (Morton 1991). We used the oscillator strengths from the Meudon group[2] based on calculations described in Abgrall et al. (1994) for H_2. We adopted the Solar abundances given by Morton (2003) based on the meteoritic data from Grevesse & Sauval (2002). For each system, the origin ($v = 0$ km s^{-1}) of the velocity scale is set to the redshift of the H_2 component.

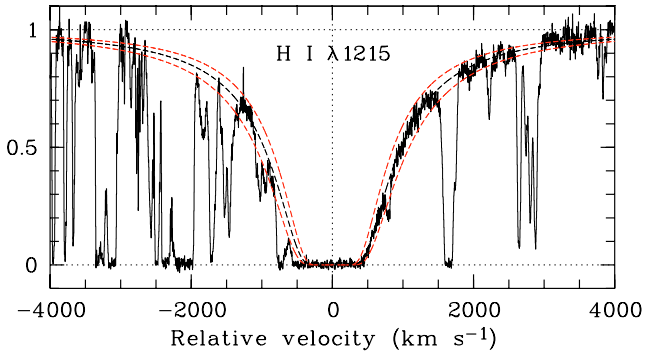

Fig. 1. Fit to the damped Lyman-α line at $z_{abs} = 2.431$ toward Q 2343+125. The derived neutral hydrogen column density is $\log N(\mathrm{H\,I}) = 20.40 \pm 0.07$. The dashed curves correspond to the best-fitted Voigt profile (black) and the associated errors (red).

3. The system at $z_{abs} = 2.431$ toward Q 2343+125

This DLA has first been studied by Sargent et al. (1988), then by Lu et al. (1996), D'Odorico et al. (2002) and Dessauges-Zavadsky et al. (2004) with high spectral resolution (∼6.5 km s^{-1}). We recently reported the detection of molecular hydrogen in this system (Petitjean et al. 2006). From Voigt-profile fitting to the H I Ly-α, β and γ lines, we find that the damped Lyman-α component is centered at $z_{abs} = 2.431$ and the column density is $\log N(\mathrm{H\,I}) = 20.40 \pm 0.07$, consistent with previous measurement by D'Odorico et al. (2002): $\log N(\mathrm{H\,I}) = 20.35 \pm 0.05$. The fit to the damped Ly-α line is shown in Fig. 1.

3.1. Molecular hydrogen and neutral carbon content

The optically thin H_2 absorption lines at $z_{abs} = 2.43128$ are very weak, i.e. close to but above the 3σ detection limit (see Fig. 2). A very careful normalization of the spectrum has been performed, adjusting the continuum locally while fitting the line profiles. We detect the first two rotational levels in this system (see Fig. 3). The total H_2 column density, integrated over the $J = 0$ and $J = 1$ rotational levels, is measured to be $\log N(H_2) = 13.69 \pm 0.09$ (12.97 ± 0.04 and 13.60 ± 0.10 for $J = 0$ and $J = 1$ respectively). This leads to an extremely small molecular fraction $\log f = \log 2N(H_2)/(2N(H_2)+N(\mathrm{H\,I})) = -6.41 \pm 0.16$. We also

[2] http://amrel.obspm.fr/molat

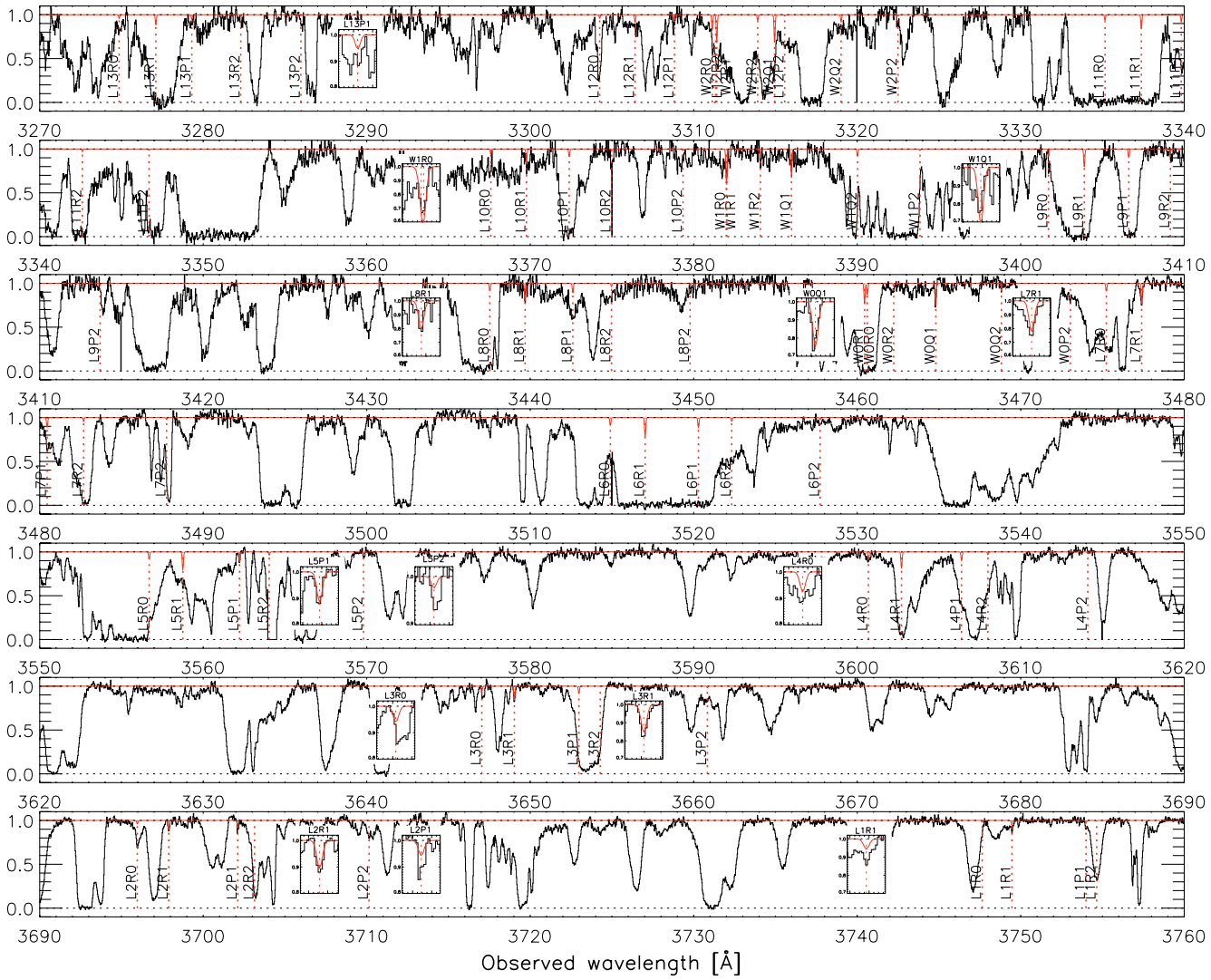

Fig. 2. Portion of the normalized spectrum of Q 2343+125. The resolving power is $R \simeq 45\,000$. The best fit to the H_2 lines is superimposed on the spectrum. Transition names are written *AxBz*, with *A* = L or W for the Lyman or Werner band systems; *x* is the quantum number of the vibrational upper state, while *B* is the branch designation (*P*, *Q* or *R* for $\Delta J = +1, 0, -1$ respectively) and *z* is the rotational quantum number of the lower state. The fit parameters are given in Table 1. Zooms into individual lines are shown in small boxes that are shifted horizontally for clarity. Each box is 0.5 Å wide.

derive a 3σ upper limit on the detection of the $J = 2$ level, $\log N(H_2, J = 2) < 13.1$, see Table 1. Neutral carbon is not detected resulting in an upper limit at 3σ: $\log N(\mathrm{C\,I}) < 12.1$. This leads to a ratio $\log N(\mathrm{C\,I})/N(H_2) < -1.6$.

3.2. Metal content

The low-ionization metal profile is spread over more than 250 km s^{-1} (Fig. 4) but shows a strong low-ionization clump on its red side. We assume that most of the metals are in this clump as it is associated with by far the strongest O I absorption feature. This main clump is itself decomposed into five components, among which the third one from the blue, at $z_{\rm abs} = 2.43129$, shows associated H_2 absorption. About 35% of Si II and S II reside in this component. The Voigt-profile fitting is shown in Fig. 5 and the corresponding parameters are given in Table 2. Note that there is very little C IV and Si IV absorption at the velocity where low-ionization metal absorptions are the strongest (see Fig. 4). High-ionization species are seen mostly blueshifted up to 300 km s^{-1} from the main low-ionization clump. It is apparent that the profile is much smoother far away from this component, suggesting a hot gas outflow.

4. The system at $z_{\rm abs} = 1.989$ toward HE 2318−1107

From Voigt-profile fitting to the H I Ly-α and Ly-β lines, we derive a total neutral hydrogen column density of $\log N(\mathrm{H\,I}) = 20.68 \pm 0.05$. The fit is shown in Fig. 6.

4.1. Molecular content

Our spectrum of HE 2318−1107 covers only a few H_2 lines, but these are unambiguously detected in a single component at $z_{\rm abs} = 1.98888$ with absorption lines from the rotational levels $J = 0$ to $J = 2$ (see Fig. 7). Some lines from the $J = 3$ level may be present but they are always blended or in regions of low SNR. We therefore derived only an upper limit at 3σ: $\log N(H_2, J = 3) < 14.7$. The results of the fit are given in Table 3. The lines are optically thin and the quality of the spectrum is high enough to measure accurate column densities in each of the

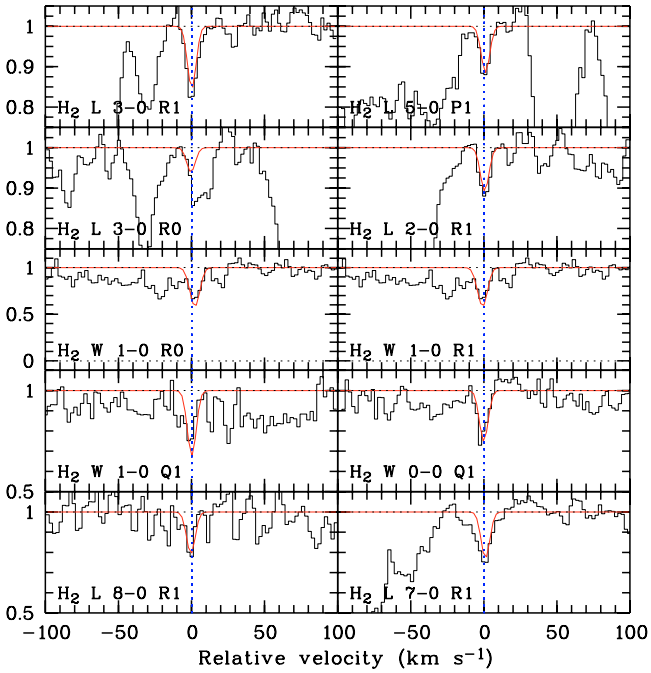

Fig. 3. Velocity plots of observed H_2 absorption lines from the $J = 0$ and $J = 1$ rotational levels at $z_{abs} = 2.43128$ toward Q 2343+125. The model fit is over-plotted.

Table 1. H_2 and C I column densities in the $z_{abs} = 2.431$ DLA toward Q 2343+125.

#[a]	z_{abs}	Level	$\log N(H_2, J)$[b]	b[c] [km s^{-1}]	T_{0-J}[d] [K]
3	2.43128(3)	$J = 0$	12.97 ± 0.04	1.3-2.6	—
		$J = 1$	13.60 ± 0.10	”	229^{+173}_{-69}
		$J = 2$	<13.10[e]	”	<420

#	z_{abs}	$\log N$(C I)	$\log N$(C I*)	b [km s^{-1}]	$\Delta v_{CI/H_2}$ [km s^{-1}]
	2.431	<12.10[e]	<12.40[e]	–	–

[a] The numbering refers to that of the metal components (see Table 2).
[b] Errors represent the allowed range for $\log N(H_2, J)$, not the rms error from the fit.
[c] Depending on the inital guess, the fit converges to two values of b, we therefore give the corresponding allowed range.
[d] The excitation temperatures between rotational levels 0 and J are calculated using the allowed range for $N(H_2, J)$.
[e] 3σ upper limit.

detected levels. The normalization of the $R \sim 54\,000$ spectrum has been done locally around each line. The total H_2 column density is $\log N(H_2) = 15.49 \pm 0.03$, leading to a low molecular fraction $\log f = -4.89 \pm 0.08$. Because $J = 1$ is mainly populated by reactive collisions, the kinetic temperature should be close to the excitation temperature $T_{01} \simeq 188$ K (Roy et al. 2006).

4.2. Neutral carbon

Neutral carbon is detected in two fine-structure levels of the ground state, $2s^2 2p^2\ ^3P_0$ (C I) and $2s^2 2p^2\ ^3P_1$ (C I*), at the same redshift as the H_2 component (see Fig. 8). A velocity shift between H_2 and C I of only 1.1 km s^{-1} is seen (see Table 3). This supports the idea that neutral carbon and molecular hydrogen absorptions originate from the same cloud. Thanks to the

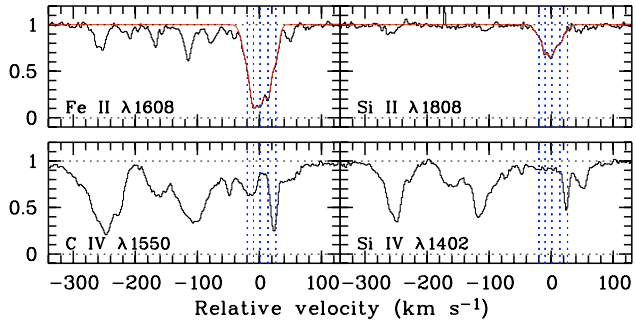

Fig. 4. Overall Si IV and C IV absorption profiles in the $z_{abs} = 2.431$ DLA toward Q 2343+125. The vertical lines mark the redshift of the main low-ionization metal components (see Table 2). Note that the C IV and Si IV absorptions from the H_2-bearing component (at $v = 0$ km s^{-1}) are absent (or weak).

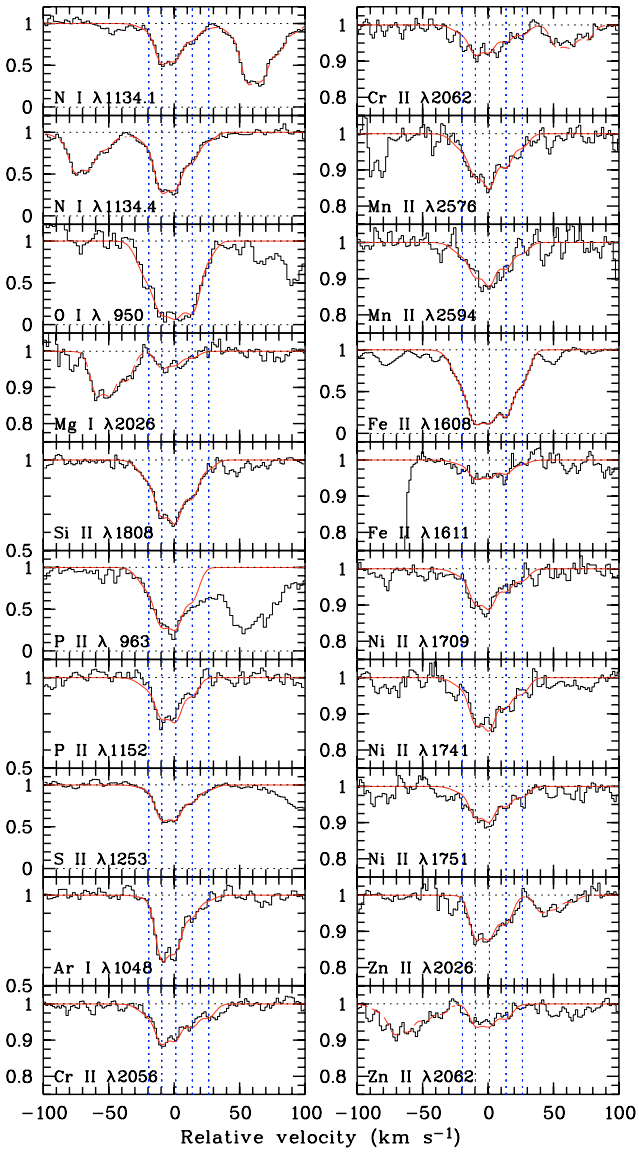

Fig. 5. Absorption profiles of low-ionization and neutral species in the damped Lyman-α system at $z_{abs} = 2.431$ toward Q 2343+125. The dotted profiles in some panels mark absorption from another element.

C I fine-structure level ratios, we can estimate the particle density in the corresponding cloud. Using a simple POPRATIO model

Table 2. Low-ionization metals column densities in the z_{abs} = 2.431 DLA toward Q 2343+125.

#	z_{abs}	Ion (X)	log N(X)	b [km s^{-1}]	$\Delta v_{X/H_2}$ [km s^{-1}]
1	2.43105(7)	N I	13.49 ± 0.02	9.3 ± 1.0	—
		O I	15.46 ± 0.02[a]	"	
		Mg I	<11.55[b]	"	
		Si II	14.31 ± 0.08	"	
		P II	12.16 ± 0.09	"	
		S II	13.41 ± 0.13	"	
		Ar I	11.64 ± 0.26	"	
		Cr II	12.00 ± 0.09	"	
		Mn II	11.51 ± 0.10	"	
		Fe II	13.57 ± 0.08	"	
		Ni II	12.39 ± 0.14	"	
		Zn II	<11.00[b]	"	
2	2.43116(9)	N I	14.20 ± 0.01	5.1 ± 0.4	—
		O I	≥15.72[c]	"	
		Mg I	11.94 ± 0.06	"	
		Si II	14.55 ± 0.07	"	
		P II	12.53 ± 0.06	"	
		S II	14.20 ± 0.04	"	
		Ar I	12.82 ± 0.02	"	
		Cr II	12.31 ± 0.06	"	
		Mn II	11.67 ± 0.08	"	
		Fe II	13.96 ± 0.05	"	
		Ni II	12.84 ± 0.06	"	
		Zn II	11.71 ± 0.04	"	
3	2.43129(3)	N I	14.19 ± 0.01	5.6 ± 0.5	+0.8
		O I	≥15.92[c]	"	
		Mg I	11.87 ± 0.08	"	
		Si II	14.70 ± 0.04	"	
		P II	12.64 ± 0.04	"	
		S II	14.24 ± 0.04	"	
		Ar I	12.78 ± 0.02	"	
		Cr II	12.34 ± 0.05	"	
		Mn II	11.89 ± 0.04	"	
		Fe II	14.00 ± 0.04	"	
		Ni II	12.97 ± 0.04	"	
		Zn II	11.74 ± 0.04	"	
4	2.43143(8)	N I	13.78 ± 0.01	5.6 ± 0.5	—
		O I	≥15.81[c]	"	
		Mg I	11.57 ± 0.13	"	
		Si II	14.45 ± 0.04	"	
		P II	12.22 ± 0.06	"	
		S II	13.88 ± 0.04	"	
		Ar I	12.32 ± 0.04	"	
		Cr II	12.14 ± 0.05	"	
		Mn II	11.66 ± 0.05	"	
		Fe II	13.90 ± 0.03	"	
		Ni II	12.71 ± 0.05	"	
		Zn II	11.57 ± 0.04	"	
5	2.43158(1)	N I	13.18 ± 0.03	5.8 ± 0.4	—
		O I	14.82 ± 0.06[a]	"	
		Mg I	<11.55[b]	"	
		Si II	13.80 ± 0.09	"	
		P II	<11.85[b]	"	
		S II	13.33 ± 0.08	"	
		Ar I	11.69 ± 0.17	"	
		Cr II	11.92 ± 0.05	"	
		Mn II	11.28 ± 0.09	"	
		Fe II	13.40 ± 0.04	"	
		Ni II	12.45 ± 0.06	"	
		Zn II	<11.00[b]	"	

[a] O I has been fitted using fixed Doppler parameters previously derived from the other ions. Errors on N(O I) could therefore be underestimated.
[b] Upper-limits are given for non-detections at the 3σ confidence level.
[c] N(O I) is considered as a lower-limit in the three saturated components because of uncertainties in the background subtraction.

(Silva & Viegas 2001), taking into account the cosmic background radiation at redshift $z \sim 2$ and using kinetic temperatures between T = 188 K and T = 300 K and a radiation field intensity between 1 and 10 times the Galactic value, leads to densities between 20 and 40 cm^{-3}. A higher UV flux would result in a lower density, whereas a lower temperature would lead to a higher density, that would be about twice higher than derived above for the mean Galactic temperature ($T \sim 77$ K; Rachford et al. 2002).

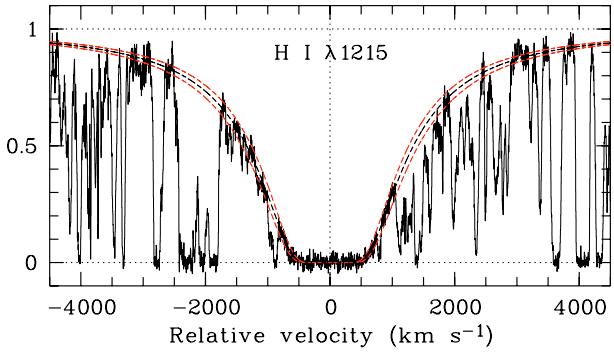

Fig. 6. Fit to the damped Lyman-α line at z_{abs} = 1.989 toward HE 2318−1107. The derived neutral hydrogen column density is log N(H I) = 20.68 ± 0.05. The dashed curves correspond to the best-fitted Voigt profile (black) and the associated errors (red).

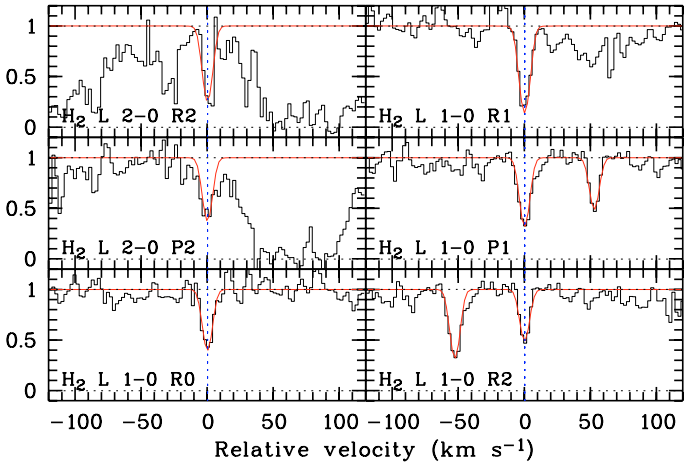

Fig. 7. H_2 absorption profile at z_{abs} = 1.98888 toward HE 2318−1107. The model fit is over-plotted.

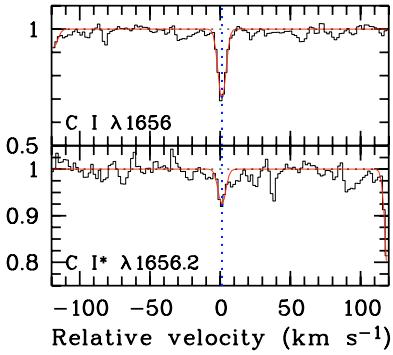

Fig. 8. C I ground-state fine-structure lines from the z_{abs} = 1.989 DLA toward HE 2318−1107.

4.3. Metal content

Ten highly blended components are needed to reproduce the whole absorption profile of low ionization species that is spread over about 200 km s^{-1} (see Fig. 9). The profile is characterized by a central and strong component which is the only one detected in H_2 and C I. S II and Si II are detected along the whole profile. The decomposition is well constrained by the Fe II λ1608 profile that is redshifted in a region with high SNR and is nowhere saturated except for the central component which is constrained by the Fe II $\lambda\lambda$2249, 2260 transition lines. Cr II, Zn II, Ni II and Mg I are detected in, respectively, seven, eight, eight and three

Table 3. H_2 and C I column densities in the $z_{abs} = 1.989$ DLA toward HE 2318−1107.

#[a]	z_{abs}	Level	$\log N(H_2, J)$[b]	b [km s^{-1}]	T^c_{0-J} [K]
5	1.98888(2)	$J = 0$	14.72 ± 0.03	3.6 ± 0.2	–
		$J = 1$	15.28 ± 0.03	”	188^{+158}_{-59}
		$J = 2$	14.84 ± 0.03	”	384^{+173}_{-91}
		$J = 3$	<14.7[d]	”	<355

#[a]	z_{abs}	$\log N$(C I)	$\log N$(C I*)	b [km s^{-1}]	$\Delta v_{C\,1/H_2}$ [km s^{-1}]
5	1.98889(3)	12.63 ± 0.02	12.30 ± 0.04	2 ± 1	+1.1

[a] The numbering refers to that of the metal components (see Table 4).
[b] The errors on the H_2 column densities are the 1σ uncertainty from fitting the Voigt-profiles.
[c] The excitation temperatures are calculated using the 3σ range for H_2.
[d] 3σ upper-limit.

components. N I is also detected over the whole profile, but because of many blends with intervening Ly-α absorptions, we consider the corresponding column densities as upper limits only, except for the central component where the column density is derived thanks to the three detected N I transitions. Mg II is also detected in the central component and possibly also in component # 9 (see Table 4). We nevertheless consider the Mg II column density in component # 9 as an upper limit because of a possible blend with Ly-α forest absorptions. Upper limits at 3σ are derived for non-detected components.

Some additional absorption is present in the blue and red wings of the Fe II λ1608 profile. Unfortunately there is no stronger Fe II absorption line in our spectrum to constrain the column densities well. If we include these wings, the total Fe II column density is increased by about 7%.

The result of Voigt-profile fitting is shown in Fig. 9 and summarized in Table 4. Summing up the column densities measured in all components, we derive a metallicity of [Zn/H] = -0.85 ± 0.06.

5. The system at $z_{abs} = 2.402$ toward HE 0027−1836

The very broad Ly-α absorption line at $z_{abs} = 2.402$ lies in the wing of the Ly-α emission line from the quasar ($z_{em} = 2.56$) where the normalization of the spectrum is problematic. We therefore fitted a Voigt-profile to the H I Ly-β line (see Fig. 10) to derive a total neutral hydrogen column density of $\log N(\mathrm{H\,I}) = 21.75 \pm 0.10$. This is one of the highest column densities measured in QSO-DLAs (see, e.g. Prochaska et al. 2005).

5.1. Molecular content

The wavelength range of the UVES spectrum allows us to observe a large number of H_2 absorption lines at the redshift of the DLA. A single H_2 component is detected in the rotational levels $J = 0$ to $J = 5$ with a possible detection of the $J = 6$ rotational level. In addition to the overall normalization of the spectrum, the continuum has been carefully normalized over about 100 to 800 km s^{-1} locally around each line. It must be noted that this system is exceptional amongst H_2-bearing DLAs, with more than 70 detected H_2 transitions. The absorption can be fitted with a single component and most of the lines are not strongly saturated. In addition, at this redshift ($z_{abs} \sim 2.4$) blending is not

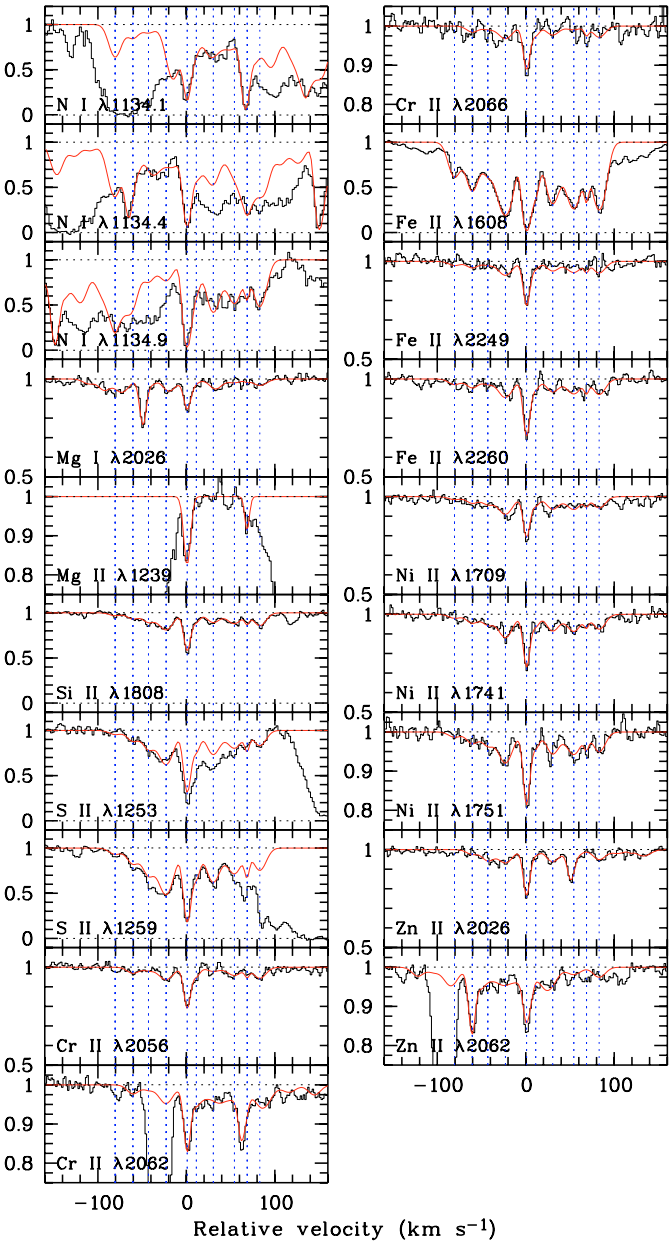

Fig. 9. Absorption profiles of low-ionization and neutral species at $z_{abs} = 1.989$ toward HE 2318−1107. Note that Mg I λ2026 is partly blended with Zn II λ2026, and so is Zn II λ2062 with Cr II λ2062. N I lines are blended altogether as well as with Ly-α forest absorptions but the column density can be derived in the central component.

strong as the Ly-α forest is not dense and the data are of high signal-to-noise ratio and high spectral resolution ($R \simeq 50\,000$). Therefore we are in an ideal position to derive with high confidence the column density N and Doppler parameter $b(J)$ for each rotational level J. The fit was performed by χ^2 minimization, considering different b-values for each rotational level. The relative optical depths of the different absorption lines with different oscillator strengths provide strong constraints on N but more importantly on b. This is particularly true for rotational levels $J = 2$ and $J = 3$ for which a large number of transitions with different oscillator strengths are observed. Some of the absorptions are in the intermediate regime where the equivalent widths strongly depend on b (corresponding to the flat part of the curve-of-growth). Note that damping wings appear for some lines of the $J = 0$ and $J = 1$ rotational levels. For the highest

Table 4. Low-ionization metals column densities in the $z_{abs} = 1.989$ DLA toward HE 2318−1107.

#	z_{abs}	Ion (X)	$\log N(X)^{a,b}$	b [km s^{-1}]	$\Delta v_{X/H_2}$ $\Delta v_{X/C\,I}$ [km s^{-1}]	#	z_{abs}	Ion (X)	$\log N(X)^{a,b}$	b [km s^{-1}]	$\Delta v_{X/H_2}$ $\Delta v_{X/C\,I}$ [km s^{-1}]
1	1.98807(8)	N I	≤14.23	8.9 ± 2.0	–	6	1.98899(3)	N I	≤13.57	4.7 ± 0.5	–
		Mg I	<11.50	”	–			Mg I	<11.50	”	–
		Mg II	blend	”				Mg II	<14.00	”	
		Si II	13.73 ± 0.06	”				Si II	14.03 ± 0.02	”	
		S II	13.33 ± 0.06	”				S II	13.87 ± 0.02	”	
		Cr II	<11.70	”				Cr II	11.94 ± 0.06	”	
		Fe II	13.52 ± 0.05	”				Fe II	13.55 ± 0.05	”	
		Ni II	<12.30	”				Ni II	12.51 ± 0.05	”	
		Zn II	<10.80	”				Zn II	10.99 ± 0.13	”	
2	1.98827(8)	N I	≤13.79	8.6 ± 0.2	–	7	1.98918(3)	N I	≤14.09	9.5 ± 1.6	–
		Mg I	<11.50	”	–			Mg I	<11.50	”	–
		Mg II	blend	”				Mg II	<14.00	”	
		Si II	14.05 ± 0.02	”				Si II	14.31 ± 0.02	”	
		S II	13.75 ± 0.02	”				S II	14.18 ± 0.02	”	
		Cr II	11.96 ± 0.08					Cr II	11.83 ± 0.11	”	
		Fe II	13.71 ± 0.04	”				Fe II	13.92 ± 0.08	”	
		Ni II	12.58 ± 0.05	”				Ni II	12.90 ± 0.02	”	
		Zn II	11.18 ± 0.12	”				Zn II	11.63 ± 0.04	”	
3	1.98845(3)	N I	≤13.53	8.4 ± 1.5	–	8	1.98942(1)	N I	≤14.01	10.5 ± 1.8	–
		Mg I	<11.50	”	–			Mg I	11.80 ± 0.13	”	–
		Mg II	blend	”				Mg II	<14.00	”	
		Si II	14.23 ± 0.05	”				Si II	14.40 ± 0.03	”	
		S II	14.00 ± 0.04	”				S II	14.07 ± 0.06	”	
		Cr II	<11.70	”				Cr II	12.17 ± 0.05	”	
		Fe II	13.43 ± 0.03	”				Fe II	14.03 ± 0.03	”	
		Ni II	12.63 ± 0.04	”				Ni II	12.96 ± 0.02	”	
		Zn II	11.53 ± 0.05	”				Zn II	11.44 ± 0.13	”	
4	1.98865(0)	N I	≤13.62	10.7 ± 4.0	–	9	1.98956(4)	N I	≤13.39	1.6 ± 1.0	–
		Mg I	<11.50	”	–			Mg I	<11.50	”	–
		Mg II	blend	”				Mg II	≤14.48	”	
		Si II	14.62 ± 0.05	”				Si II	13.85 ± 0.08	”	
		S II	14.43 ± 0.05	”				S II	13.61 ± 0.08	”	
		Cr II	12.37 ± 0.03	”				Cr II	<11.70		
		Fe II	14.13 ± 0.02	”				Fe II	13.42 ± 0.04	”	
		Ni II	13.11 ± 0.02	”				Ni II	<12.30	”	
		Zn II	11.72 ± 0.04	”				Zn II	<10.80	”	
5	1.98888(9)	N I	14.55 ± 0.02	4.2 ± 0.3	+0.7	10	1.98970(7)	N I	≤14.01	9.2 ± 1.9	–
		Mg I	12.32 ± 0.05	”	−0.4			Mg I	12.04 ± 0.08	”	–
		Mg II	14.94 ± 0.04	”				Mg II	blend	”	
		Si II	14.72 ± 0.01	”				Si II	14.42 ± 0.03	”	
		S II	14.50 ± 0.04	”				S II	13.95 ± 0.04	”	
		Cr II	12.60 ± 0.01	”				Cr II	12.26 ± 0.04	”	
		Fe II	14.35 ± 0.01	”				Fe II	13.99 ± 0.08	”	
		Ni II	13.18 ± 0.01	”				Ni II	12.84 ± 0.03	”	
		Zn II	11.97 ± 0.01	”				Zn II	11.53 ± 0.05	”	

[a] 3σ upper-limits are derived for non detected components, and marked by “<”.
[b] Components for which the column density is uncertain because of possible blends are considered as upper-limits, and marked by “≤”.

rotational levels ($J = 4$ and $J = 5$), absorption lines are optically thin, making b slightly less constrained than for lower rotational levels. However, it is apparent that these lines are broader than the $J = 2$ and $J = 3$ features. Two consistent absorption features are detected for rotational level $J = 6$, but the lines are too weak to perform a fit with an independent b. We therefore have chosen to fix $b(J = 6)$ equal to $b(J = 5)$ previously measured independently. The derived $J = 6$ column density should be preferably considered as an upper limit due to possible blends (see Table 5).

The results of the Voigt-profile fitting are shown in Figs. 19 to 25 and summarized in Table 5. The molecular fraction in this system is $\log f = -4.15 \pm 0.17$. The important finding here is that the Doppler parameter b increases with J.

5.2. Neutral carbon

Neutral carbon is detected in one component at about the same redshift as the H_2 component. The absorption line is optically

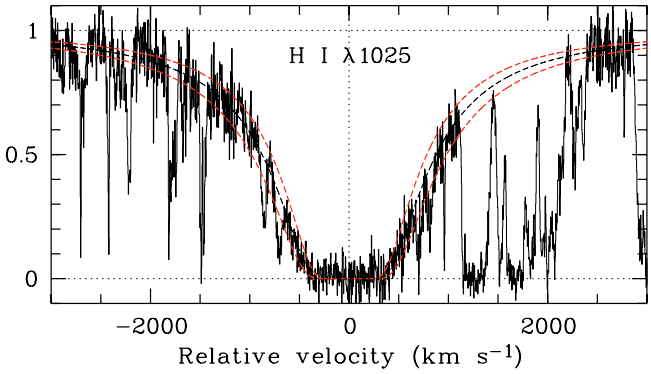

Fig. 10. Fit to the Ly-β line at $z_{abs} = 2.402$ toward HE 0027−1836. The neutral hydrogen column density is $\log N(\mathrm{H\,I}) = 21.75 \pm 0.10$. The dashed curves correspond to the best-fitted Voigt profile (black) and the associated errors (red).

Table 5. H_2 and C I column densities in the $z_{abs} = 2.402$ DLA toward HE 0027−1836.

#[a]	z_{abs}	Level	$\log N(H_2, J)$ [b]	b [km s^{-1}]	T_{0-J} [c] [K]
3	2.40183(4)	$J = 0$	16.75 ± 0.06	1.06 ± 0.13	–
		$J = 1$	17.15 ± 0.07	1.46 ± 0.14	134^{+317}_{-55}
		$J = 2$	14.91 ± 0.02	2.67 ± 0.08	88^{+9}_{-8}
		$J = 3$	14.91 ± 0.01	3.77 ± 0.07	141^{+10}_{-9}
		$J = 4$	14.22 ± 0.01	4.61 ± 0.25	213^{+14}_{-12}
		$J = 5$	14.02 ± 0.03	6.17 ± 0.69	262^{+18}_{-16}
		$J = 6$	≤13.53	6.17[d]	≤375

#[a]	z_{abs}	$\log N(\mathrm{C\,I})$	$\log N(\mathrm{C\,I^*})$	b [km s^{-1}]	$\Delta v_{\mathrm{C\,I}/H_2}$ [km s^{-1}]
3	2.40185(8)	$12.25^{+0.09}_{-0.15}$	≤12.27	0.6–3.0	+2.1

[a] The numbering refers to that of the metal components (see Table 6).
[b] The error on the H_2 column densities are the 1σ uncertainty from fitting the Voigt-profiles.
[c] The excitation temperatures are calculated using the 3σ range for $\log N(H_2, J)$.
[d] The Doppler parameter for $J = 6$ has been fixed to be equal to $b(J = 5)$ derived independently.

thin, and the column density therefore does not depend much on b. The corresponding C I* absorption is weak and detected just above the 3σ confidence level ($\log N(\mathrm{C\,I^*}) = 12.2$). The derived column density is thus uncertain and should be considered as an upper limit: $\log N(\mathrm{C\,I^*}) \leq 12.27$ (see Table 5). We observe a small velocity shift between the positions of the C I and H_2 components but no velocity shift between C I and component #3 of the low-ionization metal profile. The upper limit on $N(\mathrm{C\,I^*})/N(\mathrm{C\,I})$ leads to an upper limit on the neutral hydrogen density, $n_H < 150$ cm^{-3}, for a typical temperature of $100 < T < 200$ K and a Galactic UV radiation field (see also Noterdaeme et al. 2007).

5.3. Metal content

The profile is made of two strong well separated features ($\Delta v \sim 25$ km s^{-1}), the first one being a blend of two components. The second feature, corresponding to the third and also the strongest component in the profile , is associated with the H_2 component but is significantly broader. We detect and measure column densities for a large number of species, namely N I, Mg I, Mg II, Si II, P II, S II, Ar I, Ti II, Cr II, Mn II, Fe II, Ni II, and Zn II. In addition, we measure 3σ upper limits on the column densities of Pb II (resp. Cu II) for each component: $\log N(\mathrm{Pb\,II}) < 11.1$ (respectively, $\log N(\mathrm{Cu\,II}) < 12.1$) from the non-detection of Pb II λ1433 at $SNR \sim 46$ (resp. Cu II λ1358; $SNR \sim 16$).

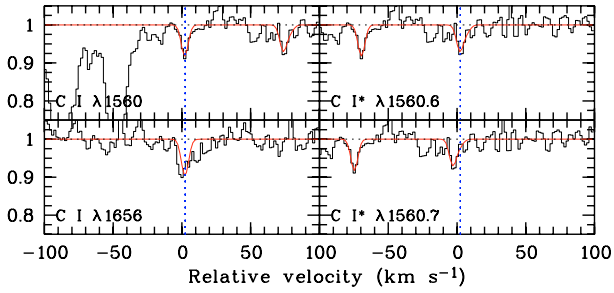

Fig. 11. Neutral carbon absorption lines toward HE 0027−1836. The C I* absorption is weak and the derived column density is thus considered as an upper limit.

To derive the characteristics of the lines, we first determined the b-values by fitting unblended and good SNR lines. We then fixed the obtained b values and added all other detected transitions. Although relative wavelengths were relaxed when fitting the lines, the final fit shows no velocity-shift between the C I component and the third metal component. Note that the best oscillator strength found in the literature for Fe II λ1112, $f = 0.00629$ (Howk et al. 2000), seems to be underestimated (see Fig. 12) unless there is extra absorption (possibly from the Ly-α forest) at that wavelength. The oscillator strength from Morton (2003) is even smaller, $f = 0.00446$. Using the measured $\lambda_{vac} = 1253.805$ for S II λ1253 (Morton 2003) induces a small but significant shift between the observed and the synthetic profiles. To make the two spectra consistent the Ritz wavelength $\lambda_{vac} = 1253.811$ (Morton 1991) had to be used instead. The metallicity derived for this system is $[\mathrm{Zn/H}] = -1.63 \pm 0.10$. A study of the highly ionized species is presented by Fox et al. (2007a,b).

5.4. C II* and the ambient UV flux

Strong and saturated C II* λ1335 absorption is seen in this system (see Fig. 13). We can use however the weaker transition at $\lambda_{rest} \simeq 1037$ Å to derive reliable column density estimates (see Table 7). During the fit redshifts of the C II* components were constrained to be the same as those of other low-ionization species. In turn, Doppler parameters could not be given the same values. In any case the b-values for C II* are not well constrained, especially for the weak component # 1 but this does not strongly affect the derived column densities. The associated uncertainties were derived by considering a range of b values. A large Doppler parameter is needed for component # 3. This probably reveals the multiple component nature of the feature. Following Wolfe et al. (2003), we can estimate the UV ambient flux in the system, considering the equilibrium between photo-electric heating and cooling by C II 158 μm emission. The heating of the gas by photo-electric effect on dust grains is proportional to the dust-to-gas ratio, ($\kappa = 10^{[\mathrm{Zn/H}]}(1 - 10^{[\mathrm{Fe/Zn}]})$), and to the UV flux, F_{UV}. The cooling rate is proportional to the C II 158 μm emission per H atom, as estimated by Pottasch et al. (1979):

$$l_c = \frac{N(\mathrm{C\,II^*})h\nu_{ul}A_{ul}}{N(\mathrm{H\,I})} \ \mathrm{erg\,s^{-1}} \ \text{per H atom}, \quad (1)$$

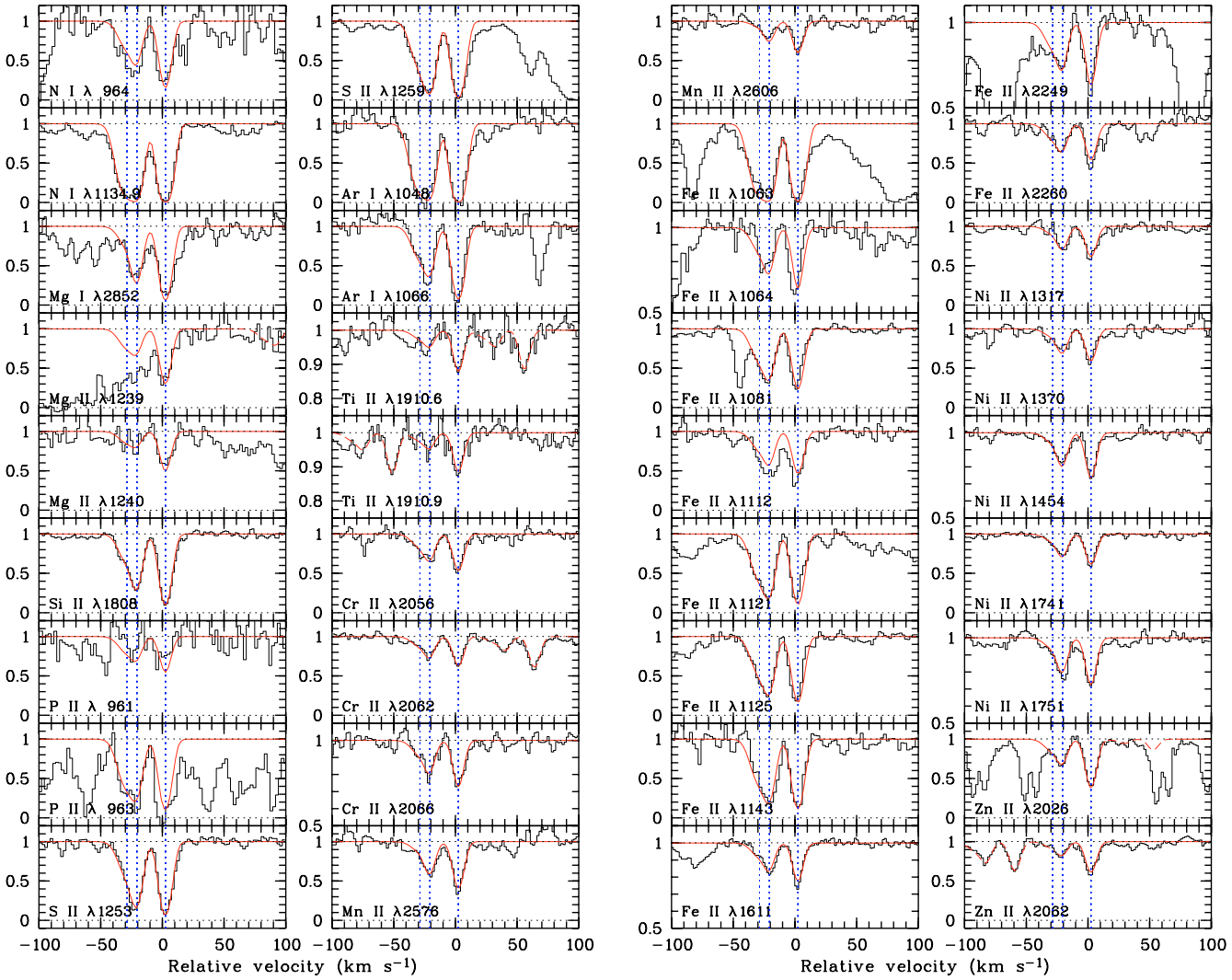

Fig. 12. Absorption profiles of low-ionization and neutral species from the $z_{abs} = 2.402$ DLA system toward HE 0027−1836. The synthetic best-fit spectrum is superimposed to the observed spectrum. The dashed lines in some panels mark absorption from another element. For example, there is some Mg I λ2026 absorption near the Zn II λ2026 one. The transitions Fe II $\lambda\lambda\lambda$1063, 1064, 1112 are shown but were not used during the fitting process because of uncertainties in atomic parameters.

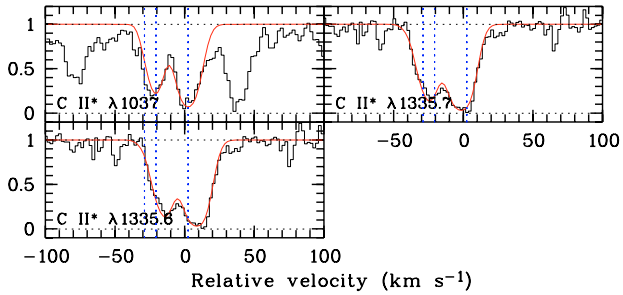

Fig. 13. C II* absorption profile in the DLA system toward HE 0027−1836. The absorption seen at $v \simeq +35$ km s^{-1} in the first panel is due to the H_2 L5–0 R1 transition.

where A_{ul} is the coefficient for spontaneous emission of the $^2P_{3/2} \rightarrow {}^2P_{1/2}$ transition and $h\nu_{ul}$ the corresponding energy. We find $\log l_c \simeq -27 \pm 0.2$. The conditions in the gas can be compared to that in the Galactic ISM, considering the same type of dust grains for both media:

$$\frac{l_c}{l_c^{gal}} \approx \kappa \frac{F_{UV}}{F_{UV}^{gal}}. \quad (2)$$

From Fig. 2 of Wolfe et al. (2003) (see also Lehner et al. 2004) it can be seen that $\log l_c^{gal} \approx -26.6$ in the Galaxy at $N(\mathrm{H\,I}) = 10^{21.75}$ cm^{-2}. We then estimate $F_{UV}/F_{UV}^{gal} \sim 20$ for $\kappa \simeq 0.02$. The UV flux in the DLA is about an order of magnitude higher than in the Galactic disk. Note that we ignored the dependence of the photo-electric heating on the temperature and density of the gas (Weingartner & Draine 2001), and that the result is therefore only valid for temperatures and densities similar to that in our Galaxy.

6. Excitation of H_2 toward HE 0027−1836

In this Section, we analyze in detail the excitation of H_2 at $z_{abs} = 2.40183$ toward HE 0027−1836 where absorptions from rotational levels $J = 1$ to $J = 5$ and possibly $J = 6$ are seen in a single component.

6.1. Excitation temperatures

Figure 14 shows the H_2 excitation diagram in this system. The graph gives for the different rotational levels $N(H_2, J)/g_J$, where

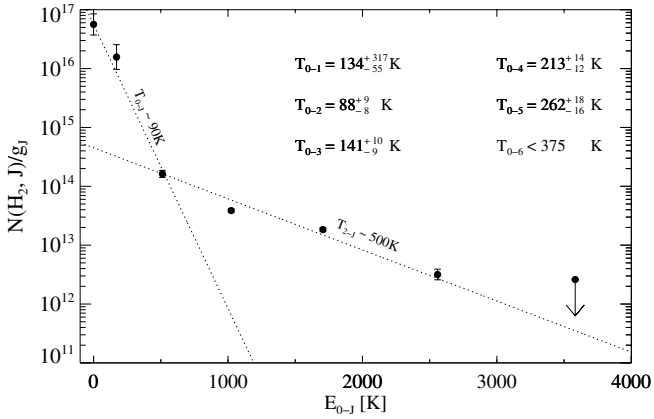

Fig. 14. Excitation diagram of H_2 at $z_{abs} = 2.40183$ toward HE 0027−1836. It is apparent that it is characterized by two excitation temperatures: $T_{0-J} \sim 90$ K for $J \leq 2$ and $T_{2-J} \sim 500$ K for $J > 2$.

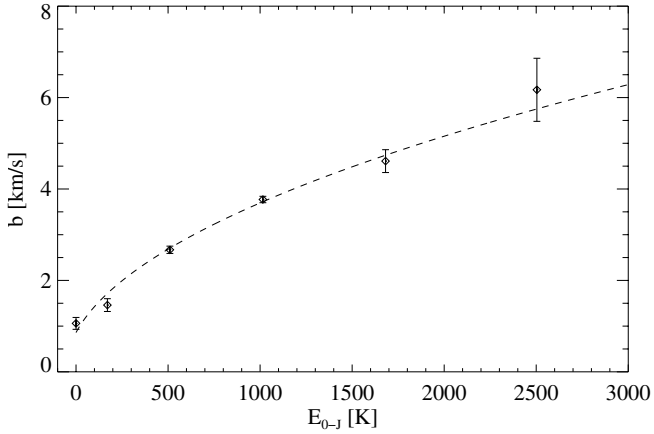

Fig. 15. The Doppler parameter b as a function of the energy between the rotational levels (from $J = 0$ to $J = 5$) in the DLA system toward HE 0027−1836. The smallest errors are found for $J = 2$ and 3, for which numerous lines with good SNR and in different optical depth regimes are observed. The dotted curve corresponds to a fit with a single free parameter (Eq. (9)).

g_J is the statistical weight of the level, versus the relative energy between that level and $J = 0$. The slope s of a straight line in the graph is inversely proportional to the excitation temperature, $s = -1/(T_{J-J'} \ln 10)$. The kinetic temperature is generally estimated by T_{0-1} assuming the $J = 1$ level is thermalised. Here, $T_{0-1} \simeq 134$ K.

The H_2 excitation diagram is characterized by two excitation temperatures, $T_{0-J} \sim 90$ K for $J \leq 2$ and $T_{2-J} \sim 500$ K for $J > 2$ (see Fig. 14). Therefore, other processes than collisions at a temperature of the order of $T \sim 100$ K (the approximate kinetic temperature) are at play. Formation pumping (just after formation, H_2 molecules are in high-J levels) and UV pumping from low-J levels upwards are likely to be the most important of these processes. Assuming these are the main processes allows us to estimate the strength of the surrounding UV radiation field. Writing the equilibrium between the processes populating and depopulating the $J = 4$ rotational level (see Eq. (5) in Noterdaeme et al. 2007, also Hirashita & Ferrara 2005; Cui et al. 2005), we can estimate the photo-absorption rate in the $J = 0$ level, β_0, inside the H_2-bearing cloud: $\beta_0 \simeq 2.5 \times 10^{-11}\,s^{-1}$. This is a very low value, probably due to self- and dust-shielding by the outer layers of the cloud. The corrective term for shielding is expressed as (Draine & Bertoldi 1996):

$$S_{\rm shield} = \left(\frac{N(H_2)}{10^{14}\,{\rm cm}^{-2}}\right)^{-0.75} {\rm e}^{-\tau_{\rm UV}}. \quad (3)$$

This is the product of two terms, the first term, S_{H_2}, is due to self-shielding, the second, $S_{\rm dust}$, is due to dust extinction. The total H_2 column density in the cloud is $N(H_2) = 10^{17.3}\,{\rm cm}^{-2}$, leading to $S_{H_2} \simeq 0.00335$. Dust extinction is calculated using the dust optical depth, $\tau_{\rm UV}$:

$$\tau_{\rm UV} = 0.879\left(\frac{a}{0.1\,\mu{\rm m}}\right)^{-1}\left(\frac{\delta}{2\,{\rm g\,cm}^{-3}}\right)^{-1}\left(\frac{g}{10^{-2}}\right)\left(\frac{N_{\rm H}}{10^{21}\,{\rm cm}^{-2}}\right) \quad (4)$$

where a is the radius of a grain, g is the dust-to-gas mass ratio and δ is the grain material density (Hirashita & Ferrara 2005). This optical depth is difficult to estimate, due to the unknown type of dust and the uncertainty on the exact H I column density in the H_2-bearing component. We can assume $a = 0.1\,\mu$m, $\delta = 2\,{\rm g\,cm}^{-3}$, and scale the dust-to-gas mass ratio g with the dust-to-gas ratio $\kappa = 10^{[{\rm Zn/H}]}\left(1 - 10^{[{\rm Fe/Zn}]}\right)$ (Prochaska & Wolfe 2002). We then get:

$$\tau_{\rm UV} = 0.879\,\kappa\left(\frac{N_{\rm H}}{10^{21}\,{\rm cm}^{-2}}\right) \quad (5)$$

or equivalently,

$$\tau_{\rm UV} = 0.879\left(\frac{N({\rm Zn})}{10^{[{\rm Zn/H}]_\odot}} - \frac{N({\rm Fe})}{10^{[{\rm Fe/H}]_\odot}}\right)\left(\frac{1}{10^{21}\,{\rm cm}^{-2}}\right) \quad (6)$$

where the column densities are those measured in the H_2-bearing component. We obtain $S_{\rm dust} = 0.94$ and $S_{\rm shield} = S_{H_2} S_{\rm dust} \simeq 0.003$. Note that the self-shielding dominates the total shielding. We can then estimate the UV flux outside the cloud (see Noterdaeme et al. 2007):

$$J_{\rm LW} \simeq \frac{8 \times 10^{-11}\beta_0}{S_{\rm shield}} \simeq 6.3 \times 10^{-19}\,{\rm erg\,s^{-1}\,cm^{-2}\,Hz^{-1}\,sr^{-1}}. \quad (7)$$

This is about 20 times higher than in the solar vicinity ($J_{{\rm LW},\odot} \simeq 3.2 \times 10^{-20}\,{\rm erg\,s^{-1}\,cm^{-2}\,Hz^{-1}\,sr^{-1}}$; Habing 1968). Again, all this assumes that the high rotational levels of H_2 are populated by formation- and UV-pumping. If collisional excitation, in case of turbulence or shocks for example, is playing an important role, then the derived UV flux should be considered as an upper limit.

6.2. Velocity dispersion

In Fig. 15, we plot the Doppler parameter of the lines from a given rotational level, b, as a function of the energy of the rotational level J. It is apparent that higher J levels have broader lines. This effect has already been observed in the local interstellar medium in some cases. It has first been derived from curve-of-growth analysis in several *Copernicus* observations (Spitzer & Cochran 1973; Spitzer et al. 1974), then observed directly by Jenkins & Peimbert (1997) with $R = 120\,000$ data from the Interstellar Medium Absorption Profile Spectrograph (IMAPS). In that case however the increase in the line broadening is associated with a regular shift in velocity. More recently, the same effect has been reported by Lacour et al. (2005) along four lines of sight toward early-type Galactic stars. In high redshift DLAs, Ledoux et al. (2003) already suggested that the lines of $J \geq 2$ rotational levels require higher b values than the lower J-level

lines. It is however the first time that a systematic effect is seen beyond any doubt at high redshift.

In case the broadening is only thermal, the Doppler parameter is related to the kinetic energy by:

$$b(J) = \sqrt{2k_{\rm B}E_k(J)/(3m_{\rm H})}. \quad (8)$$

If we assume that the excess of kinetic energy of molecules in some J level compared to the kinetic energy of molecules in the $J = 0$ level is directly proportional to the energy of the rotational level, i.e. $E_k(J) - E_k(0) = a\,E_{0-J}$, with a a constant, then we can try to fit the observed trend with the expression:

$$b(J) = \sqrt{2k_B(E_k(0) + a\,E_{0-J})/\,(3m_{\rm H})} \quad (9)$$

where $E_k(0)$ is the kinetic energy of rotational level $J = 0$, for which we use the excitation temperature $T_{0-1} \simeq 134$ K previously determined. The least square minimization gives $E_k(J) \simeq E_k(0) + 2.34\,E_{0-J}$. The result is shown in Fig. 15. One can see that this very simple assumption fits the data very well. It is not easy to find an explanation to this effect. Jenkins & Peimbert (1997) argued that such trend in b seen along the line of sight to χOriA could be explained if the gas is located behind a J-shock. However, the column densities along the present line of sight are much larger and, more importantly, this would produce coherent velocity shifts between the lines from different J levels, which we do not observe.

UV pumping cannot produce different b values because the cascade following the UV absorption releases the energy through infrared photons, and such process does not result in any change in the molecule's kinetic energy.

Lacour et al. (2005) show that such behavior can be explained by the consequences of H_2-formation onto dust grains. After formation, the molecules escape with an excess kinetic energy left-over from the formation process. The highest rotational levels have a radiative life-time considerably shorter than the lowest J levels. This implies that low-J molecules have more time than high-J molecules to cool down through collisions with H I (see, e.g., Spitzer & Cochran 1973; Lacour et al. 2005). This implies that, if other processes are negligible, the kinetic energy of high-J molecules could be larger than that of low-J ones. It can be seen in Fig. 6 of Lacour et al. (2005) that their model approximately reproduces the values measured here. However, their model requires a formation rate ∼10 times higher than that measured in the Galactic ISM (Jura 1975; Gry et al. 2002). It is clear that at the low metallicity measured in the present DLA system, [Zn/H] = −1.63, this assumption can be rejected.

Another explanation could be that the cloud is composed of several layers with a gradient of temperature. External layers would be warm and exposed to strong external UV flux. In these layers, the excitation of H_2 could be large and mostly due to UV pumping. They would contribute mostly to the column densities of high J-levels. The internal layers would be cold and shielded from the external UV flux. It must be realized that the increased b with higher J is coupled with an excitation diagram described by two excitation temperatures, $T_{0-J} \sim 90$ K for $J = 0$–2 and $T_{2-J} \sim 500$ K for $J = 3$–6 (see Fig. 14). This kind of diagram has been explained in the Galactic ISM by invoking the association of a diffuse cold cloud with a warm Photo-Dissociation Region (PDR), see Boissé et al. (2005).

6.3. Models

We used the Meudon PDR code (Le Petit et al. 2006; Goicoechea & Le Bourlot 2007) to model the system toward HE 0027−1836 where H_2 is detected in rotational levels $J = 0$ to $J = 5$. This PDR model assumes a stationary plan-parallel slab of dust and gas of constant hydrogen density $n_{\rm H}$, illuminated by a UV radiation field and solves the radiative transfer, chemistry and thermal balance. The code used in this paper is a slightly modified version compared to the online one[3]. We adopt the Interstellar Radiation Field (ISRF) as given by Draine (1978), scaled by a factor χ. Note that the energy between 912 and 2400 Å for the Draine ISRF is 1.78 times that of the Habing radiation field. The grain size distribution is assumed to follow the Mathis et al. (1977) law with radii between 0.1 and 0.3 μm. The mean Galactic dust extinction curve is used. Elemental abundances for C, N, O and S are scaled from solar abundances, $[{\rm X/H}]_\odot$, of Morton (2003), using the observed sulfur metallicity, [S/H] (see Table 6).

Savage & Sembach (1996) have shown, in the context of diffuse Galactic clouds, that depletion varies significantly from one line of sight to another. Here, we test two extreme assumptions to fix the gas phase abundances of C and O: the same

Table 6. Low-ionization metals column densities in the $z_{\rm abs} = 2.402$ DLA toward HE 0027−1836.

#	$z_{\rm abs}$	Ion (X)	$\log N$(X)	b [km s^{-1}]	$\Delta v_{\rm X/H_2}$ $\Delta v_{\rm X/C\,I}$ [km s^{-1}]
1	2.40150(4)	N I	14.53 ± 0.24	8.4 ± 1.5	–
		Mg I	11.52 ± 0.09	”	–
		Mg II	15.32 ± 0.14	”	
		Si II	14.84 ± 0.11	”	
		P II	12.62 ± 0.30	”	
		S II	14.41 ± 0.10	”	
		Ar I	13.64 ± 0.06	”	
		Ti II	11.87 ± 0.29	”	
		Cr II	12.71 ± 0.04	”	
		Mn II	11.93 ± 0.16	”	
		Fe II	14.36 ± 0.05	”	
		Ni II	12.88 ± 0.10	”	
		Zn II	11.99 ± 0.10	”	
2	2.40159(6)	N I	14.51 ± 0.22	4.7 ± 0.9	–
		Mg I	11.96 ± 0.09	”	–
		Mg II	15.14 ± 0.17	”	
		Si II	15.06 ± 0.07	”	
		P II	12.50 ± 0.30	”	
		S II	14.68 ± 0.03	”	
		Ar I	13.64 ± 0.06	”	
		Ti II	11.90 ± 0.11	”	
		Cr II	12.81 ± 0.04	”	
		Mn II	12.31 ± 0.08	”	
		Fe II	14.39 ± 0.05	”	
		Ni II	13.21 ± 0.05	”	
		Zn II	12.09 ± 0.06	”	
3	2.40185(8)	N I	15.04 ± 0.09	4.7 ± 0.2	+2.1
		Mg I	12.41 ± 0.05	”	0.0
		Mg II	15.81 ± 0.02	”	
		Si II	15.45 ± 0.02	”	
		P II	12.87 ± 0.40	”	
		S II	14.98 ± 0.03	”	
		Ar I	14.24 ± 0.02	”	
		Ti II	12.41 ± 0.03	”	
		Cr II	13.08 ± 0.01	”	
		Mn II	12.60 ± 0.02	”	
		Fe II	14.66 ± 0.03	”	
		Ni II	13.42 ± 0.02	”	
		Zn II	12.60 ± 0.01	”	

[3] http://aristote.obspm.fr/MIS

depletion on dust as in the cool medium towards ζ Oph (Savage & Sembach 1996) or no depletion. This gives in the first case C/H = 2.35×10^{-6} and O/H = 3.9×10^{-6} and in the second case 6.2×10^{-6} and 1.0×10^{-5}, respectively. CMB temperature is assumed to be 9.2 K ($z = 2.4$). We built two grids of models: one corresponding to isothermal models with $T_{\rm gas} = 130$ K corresponding to the observed value of T_{0-1} and one corresponding to models solving the thermal balance equations. For each grid we compute models with $\chi = 1$, 10, 20, 30 and $n_{\rm H} = 10$, 100, 150, 200, 400, 500 cm^{-3}. We checked the influence of the dust-to-gas mass ratio, g, or equivalently $C_{\rm D} = N_{\rm H}/E(B-V)$, the ratio of total neutral hydrogen column density to color excess, using $g = 0.01$ and $C_{\rm D} = 5.8 \times 10^{21}$ (corresponding to the ISM values; Bohlin et al. 1978), 0.001, 5.8×10^{22} and 0.0001, 5.8×10^{23} cm^{-2} mag^{-1}. Column densities are computed perpendicular to the plane parallel slab. Since the size of the cloud is not known, all models assume a semi-infinite geometry up to reproduce half of the observed $N(H_2)$. Then column densities are multiplied by 2 to simulate a slab of gas illuminated on both sides. The model is constrained by the condition that the total observed $N(H_2)$ should be reproduced.

The best iso-thermal models are obtained with $g = 0.001$ and $C_{\rm D} = 5.8 \times 10^{22}$ cm^{-2} mag^{-1} corresponding, as expected, to a low dust content (note that if we scale depletion with the observed [Zn/Cr] ratio, see previous section, we obtain $g = 0.002$). Figure 16 presents the excitation diagrams obtained with isothermal assumption in two cases. The best fit to the data for all levels is obtained with $n_{\rm H} = 150$ cm^{-3}, $\chi = 10$ (about 20 times the Habing radiation field). This model reproduces reasonably well all column densities except that of the $J = 2$ level which is overestimated by nearly an order of magnitude. The low observed value of $N(J = 2)$ relative to other column densities is the special feature of this DLA system. In this model, the molecular fraction is $f = 10^{-4}$ so H is the main collisional partner for H_2. It must be noted that H/H_2 collision rates are poorly known mainly because of reactive collisions. However using collision rates from Flower & Roueff (1998) instead of those from Mandy & Martin (1993) does not change the results significantly. Amongst models of total H_2 column density corresponding to the observed one, only those with low-density, $n_{\rm H} \simeq 10$ cm^{-3}, and weak radiation field, $\chi \simeq 1$ (Fig. 16), can reproduce the observed $N(H_2, J = 2)$. Higher densities tend to thermalize $J = 2$ whereas higher radiation fields tend to pump this level too much. The influence of the distribution of H_2 amongst ro-vibrational levels after formation on dust has also been tested. It can be noted that a few lines of sight with $T_{0-2} \leq T_{0-1}$ have been observed by FUSE and Copernicus in our Galaxy or the Magellanic clouds. The HD 108927 line-of-sight has been modelled by Gry et al. (2002). The authors reached similar conclusions. However, with such low density and UV flux ($n_{\rm H} \simeq 10$ cm^{-3}, $\chi = 1$), populations of $J > 2$ levels will be under-estimated by more than one order of magnitude. Note, however, that in these models, N(C I) and N(C I*) are in good agreement with observations. Depending on the adopted depletion of C into dust grains, N(C II*), N(C I) and N(C I*) are reproduced within a factor of 2 to 3 which is acceptable considering the uncertainties in the model. N(S II), N(Mg I) and N(Mg II) are also in good agreement with observations.

Thermal balance models lead to similar conclusions. These models are, in principle, more constrained as they have to reproduce T_{0-1}. However, they are dependent on assumptions on (i) the dust composition since the photo-electric effect on dust is the main heating mechanism and (ii) the elemental abundance of oxygen which controls cooling. Best model is again for $g = 0.001$ and $C_{\rm D} = 5.8 \times 10^{22}$ cm^{-2} mag^{-1}. As for isothermal models, a low density is required to avoid to overestimate $N(H_2, J = 2)$. With the first set of abundances (same depletion as in the cool medium towards ζ Oph), the best model is $n_{\rm H} = 50$ cm^{-3} and $\chi = 1$. In this case, $T_{0-1} = 90$ K. A lower density of 10 cm^{-3} increases T_{0-1} to 180 K because of the low abundance of coolants. With the second set of abundances (no depletion), $n_{\rm H} = 10$ cm^{-3} and $\chi = 1$ is favored and gives $T_{0-1} = 96$ K. The corresponding excitation diagrams are presented in Fig. 17.

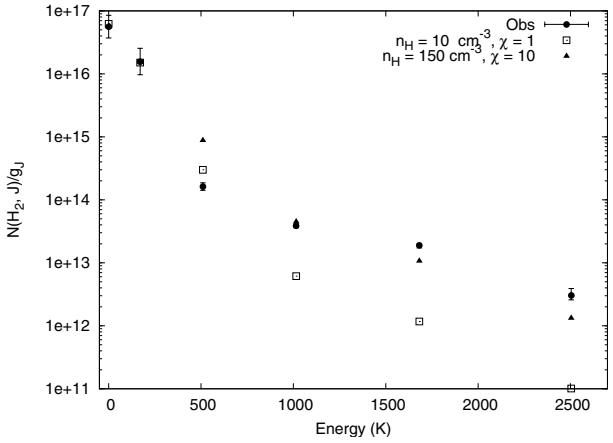

Fig. 16. Excitation diagrams obtained for isothermal models with $T_{\rm gas} = 130$ K. Grain parameters are $g = 0.001$ and $C_{\rm D} = 5.8 \times 10^{22}$ cm^{-2} mag^{-1}.

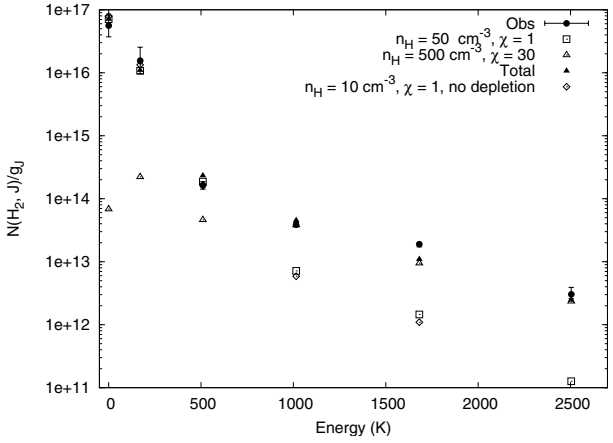

Fig. 17. Excitation diagrams obtained with thermal balance models. Grains parameters are $g = 0.001$ and $C_{\rm D} = 5.8 \times 10^{22}$ cm^{-2} mag^{-1}.

In the two models, T_{0-1} is representative of the kinetic temperature which varies from about 100 to 88 K when the depth in the cloud increases. The best-fit model with a depletion following that towards ζ Oph gives N(C II*) = 5×10^{13}, N(C I) = 8.0×10^{11} and N(C I*) = 7.8×10^{11} cm^{-2}. The one with no depletion gives 1.4×10^{14}, 5.8×10^{12} and 3.2×10^{12} cm^{-2} for the same species. Both models are within a factor of two from observations (see Tables 7 and 5). The population of high-J levels cannot be reproduced by the above low-density models and a PDR component has to be added. High density and strong radiation field are required in order to explain H_2 excitation by fluorescence. Figure 17 gives an example in which the high-J populations are produced in a clump of density $n_{\rm H} = 500$ cm^{-3} with $\chi = 30$. The corresponding size is 0.3 pc. Note that the value of the UV radiation field intensity is consistent with what is estimated analytically in Sects. 6.1 and 5.4.

Table 7. C II* column densities in the z_{abs} = 2.402 DLA toward HE 0027−1836.

#[a]	z_{abs}	log N(C II*)	b [km s^{-1}]
1	2.40150(4)	12.65 ± 0.30	3–8
2	2.40159(6)	13.80 ± 0.10	4–7
3	2.40185(8)	14.15 ± 0.25	7–9

[a] The numbering refers to that of the low-ionization metal components (see Table 6).

However, the probability that the line of sight crosses such a clump is small especially when the model requires that this small clump must be embedded in a particularly strong UV radiation field. Note also that there is no velocity shift between the absorption lines of the different J levels suggesting that they are not produced in very different locations. Another possibility to explain the excitation is turbulent dissipation either as vortices or C-shocks (Joulain et al. 1998; Cecchi-Pestellini et al. 2005; Gredel et al. 2002; Le Petit et al. 2004). In that case, increased temperature in turbulent vortex would be responsible for the excitation of the higher H_2 rotational levels. Indeed, Joulain et al. (1998) show that there should be no shift between the centroids of different species and that the widths of the lines should be larger for higher excitation as observed in the present case. Cecchi-Pestellini et al. (2005) show that a small amount of hot gas located in turbulent dissipative cells can explain the H_2 excitation. However, temperature excitation as high as T_{2-J} = 500 K for a low total $N(H_2, J > 2)$ may be difficult to be reproduced by such models. This assumption probably deserves more detailed investigation.

7. Comments on metallicity and depletion

In Fig. 18, we compare the depletion patterns for the three systems presented here to the typical depletions observed in cold and warm gas of the Galactic disk and gas in the Galactic halo. The different points correspond to the different components in each system in which Zn II is detected. It is apparent that the Galactic halo depletion pattern represents best the observed abundances. The differences between components are small. In the DLA system toward HE 0027−1836, the depletion found in the H_2-component is the highest in the system however: [Zn/Cr] = 0.54, while it is ∼0.3 in the other components. Similarly, [Zn/Fe] = 0.77 in the H_2-bearing component, while [Zn/Fe] = 0.46 and 0.53 in the other two components. Note that silicon is almost non-depleted in all components of the three systems. This is similar to what is observed through some lines of sight in the Small Magellanic Cloud (Welty et al. 2001). The small depletion factor, together with low metallicities, implies that the dust content is small and can explain the low observed molecular fraction. The fact that we do not detect H_2 in other components cannot only be due to the little difference in dust-to-gas ratio, resulting in a lower H_2 formation rate. The main reason is probably the lower column densities in the components (especially for HE 2318−1107). We summarize the total abundances found in the three systems in Table 8.

8. Conclusion

We have presented a detailed analysis of three H_2-bearing damped Lyman-α systems. Two of them are reported here for the first time. This brings the number of known high-redshift

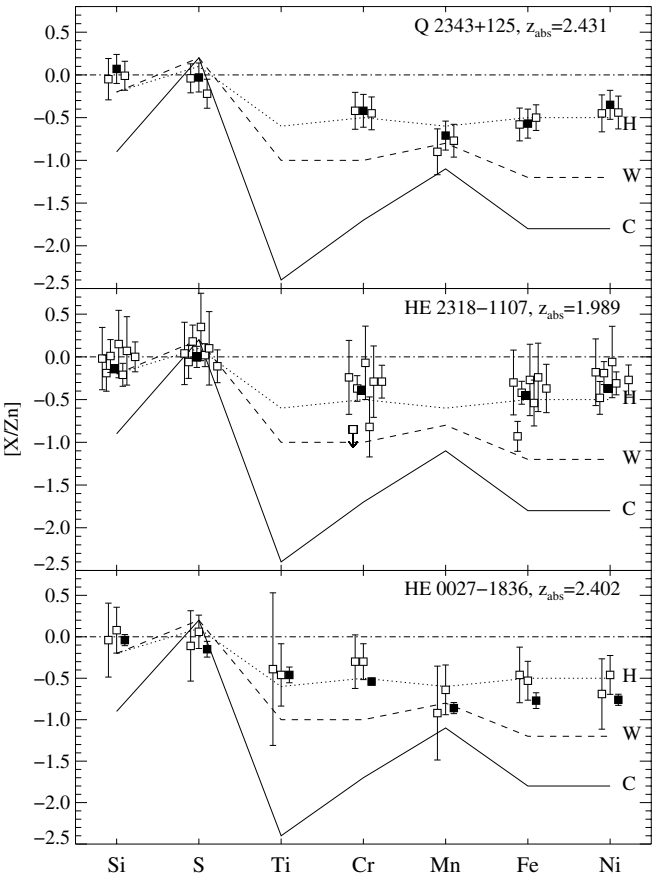

Fig. 18. Depletion pattern for the three systems presented in this paper. The solid, dashed and dotted lines, represent the typical relative abundances observed in, respectively, cold (C) and warm (W) gas in the Galactic disk and diffuse gas in the Galactic halo (H), from Welty et al. (1999). The dashed-dotted line corresponds to solar abundances. Filled squares stand for H_2-bearing components, open squares for other components in the system. We show only the components in which Zn II is detected. For each system, components are shifted in abscissa according to their redshift (i.e., the bluest components are on the left). It is apparent that the Galactic halo depletion pattern represents best the observed abundances. There is no significant difference between H_2-components and the other components although it seems that depletion (from Cr II, Mn II, Fe II, and Ni II) is slightly higher in the H_2 component of the DLA toward HE 0027−1836.

($z_{abs} > 1.8$) H_2-bearing DLAs to twelve. All three systems have low-molecular fractions ($\log f \leq -4$). Only one DLA system with such a low molecular fraction was reported before, at z_{abs} = 3.025 toward Q 0347−383 (Levshakov et al. 2002).

The depletion patterns observed in the components of the three systems are very similar to what is observed in gas located in the Galactic halo, probably because of similarly low metallicities. The depletion is not very different, although slightly larger, in the H_2-bearing components compared to the other components in the systems. This is different from what is seen in systems with larger molecular fractions where large depletion factors are usually observed in H_2-bearing components (Ledoux et al. 2003; Rodríguez et al. 2006). This could be a consequence of the relation between molecular fraction and metallicity (Petitjean et al. 2006).

The system toward HE 0027−1836 is particularly interesting as it shows absorption from rotational levels J = 0 to 5 (and possibly J = 6) in a single well-defined component. The UV radiation field intensity in which this system is immersed is found

Table 8. Summary of metals abundances in newly discovered H_2-bearing DLAs.

QSO	Q 2343+125, z_{em} = 2.51		HE 2318−1107, z_{em} = 2.96		HE 0027−1836, z_{em} = 2.56	
z_{abs}	2.431		1.989		2.402	
log N(H I)	20.40 ± 0.07		20.68 ± 0.05		21.75 ± 0.10	
log $N(H_2)$	13.69 ± 0.09		15.49 ± 0.03		17.30 ± 0.07	
log f	−6.41 ± 0.16		−4.89 ± 0.08		−4.15 ± 0.17	
Ion (X)	log N(X)	[X/H]	log N(X)	[X/H]	log N(X)	[X/H]
N I	14.62 ± 0.01	−1.73 ± 0.07	>14.55[a]	>−2.08[a]	15.25 ± 0.08	−2.45 ± 0.13
Mg I	12.40 ± 0.15		12.73 ± 0.11		12.58 ± 0.04	
Mg II	<14.69	<−1.29	>14.94[b]	>−1.32[b]	16.00 ± 0.04	−1.33 ± 0.11
Si II	15.15 ± 0.03	−0.81 ± 0.08	15.34 ± 0.01	−0.90 ± 0.05	15.67 ± 0.03	−1.64 ± 0.10
P II	13.05 ± 0.03	−0.91 ± 0.08	–	–	13.17 ± 0.23	−2.14 ± 0.25
S II	14.66 ± 0.02	−0.94 ± 0.07	15.09 ± 0.02	−0.79 ± 0.05	15.23 ± 0.02	−1.72 ± 0.10
Ar I	13.19 ± 0.01	−1.61 ± 0.07	–	–	14.42 ± 0.02	−1.73 ± 0.10
Ti II	<11.85	<−1.49	<12.00	<−1.62	12.61 ± 0.06	−2.08 ± 0.12
Cr II	12.87 ± 0.03	−1.22 ± 0.08	13.13 ± 0.06	−1.24 ± 0.08	13.37 ± 0.01	−2.07 ± 0.10
Mn II	12.35 ± 0.03	−1.58 ± 0.08	–	–	12.84 ± 0.03	−2.44 ± 0.10
Fe II	14.52 ± 0.02	−1.38 ± 0.07	14.91 ± 0.01	−1.27 ± 0.05	14.97 ± 0.02	−2.28 ± 0.10
Ni II	13.43 ± 0.03	−1.22 ± 0.08	13.82 ± 0.03	−1.11 ± 0.06	13.70 ± 0.02	−2.30 ± 0.10
Zn II	12.20 ± 0.07	−0.87 ± 0.10	12.50 ± 0.03	−0.85 ± 0.06	12.79 ± 0.02	−1.63 ± 0.10

[a] Because of many blends, we take N(N I) in the central component as a lower limit on the total neutral nitrogen column density.
[b] Considering only N(Mg II) in the main component since the other components are either blended with Ly-α forest absorptions or not detected.

to be about 20 times the Galactic ambient flux. This could be an upper limit as it is estimated assuming that H_2 excitation is mainly due to UV pumping. However the same value is found when estimating the cooling rate in the gas from the C II* column density.

Thanks to the very high data quality, we observe for the first time at high z an increase of the Doppler parameter b from low to high H_2 rotational levels. To the first approximation, there is a linear relation between the kinetic energy of the molecule (as given by the Doppler parameter) and the energy of the rotational levels. The explanation that this is a direct consequence of the formation of H_2 onto dust-grains (see Lacour et al. 2005) is difficult to accommodate given the low formation rate in the DLA gas due to low metallicity and small dust-to-gas ratio.

Detailed PDR models have been constructed to reproduce the observations in this system that is special because of the low $N(H_2, J = 2)$ column density compared to other J level column densities. Two components are needed, one with low particle density and weak radiation field to reproduce $J \leq 2$ levels column densities and one with high density and strong radiation field for $J > 2$ levels. This combination may appear ad-hoc but is unavoidable in the context of PDR models. On the other hand, the Doppler broadening and the excitation of H_2 can also be explained by increased temperature in part of the gas due to turbulent dissipation or C-shocks (Joulain et al. 1998; Cecchi-Pestellini et al. 2005; Lacour et al. 2005), as supported by the small depletion, the low molecular fraction and the small, if any, velocity shift between H_2 and C I absorptions.

Acknowledgements. We thank the anonymous referee for useful comments. PN is supported by a Ph.D. fellowship from ESO. P.P.J. and R.S. gratefully acknowledge support from the Indo-French Centre for the Promotion of Advanced Research (Centre Franco-Indien pour la Promotion de la Recherche Avancée) under contract No. 3004-3.

References

Abgrall, H., Roueff, E., Launay, F., & Roncin, J.-Y. 1994, Canadian J. Phys., 72, 856
Ballester, P., Modigliani, A., Boitquin, O., et al. 2000, The Messenger, 101, 31
Black, J. H., Chaffee, F. H., & Foltz, C. B. 1987, ApJ, 317, 442
Bohlin, R. C., Savage, B. D., & Drake, J. F. 1978, ApJ, 224, 132
Boissé, P., Le Petit, F., Rollinde, E., et al. 2005, A&A, 429, 509
Cecchi-Pestellini, C., Casu, S., & Dalgarno, A. 2005, MNRAS, 364, 1309
Cui, J., Bechtold, J., Ge, J., & Meyer, D. M. 2005, ApJ, 633, 649
Dekker, H., D'Odorico, S., Kaufer, A., Delabre, B., & Kotzlowski, H. 2000, in Optical and IR Telescope Instrumentation and Detectors, ed. M. Iye, & A. F. Moorwood, Proc. SPIE, 4008, 534
Dessauges-Zavadsky, M., Calura, F., Prochaska, J. X., D'Odorico, S., & Matteucci, F. 2004, A&A, 416, 79
D'Odorico, V., Petitjean, P., & Cristiani, S. 2002, A&A, 390, 13
Draine, B. T. 1978, ApJS, 36, 595
Draine, B. T., & Bertoldi, F. 1996, ApJ, 468, 269
Flower, D. R., & Roueff, E. 1998, J. Phys. B Atom. Mol. Phys., 31, L955
Fox, A. J., Ledoux, C., Petitjean, P., & Srianand, R. 2007a, A&A, in press [arXiv:0707.4065]
Fox, A. J., Petitjean, P., Ledoux, C., & Srianand, R. 2007b, A&A, 465, 171
Goicoechea, J. R., & Le Bourlot, J. 2007, A&A, 467, 1
Gredel, R., Pineau des Forêts, G., & Federman, S. R. 2002, A&A, 389, 993
Grevesse, N., & Sauval, A. J. 2002, Adv. Space Res., 30, 3
Gry, C., Boulanger, F., Nehmé, C., et al. 2002, A&A, 391, 675
Habing, H. J. 1968, Bull. Astron. Inst. Netherlands, 19, 421
Hirashita, H., & Ferrara, A. 2005, MNRAS, 356, 1529
Hollenbach, D., & Salpeter, E. E. 1971, ApJ, 163, 155
Howk, J. C., Sembach, K. R., Roth, K. C., & Kruk, J. W. 2000, ApJ, 544, 867
Jenkins, E. B., & Peimbert, A. 1997, ApJ, 477, 265
Jenkins, E. B., & Tripp, T. M. 2006, ApJ, 637, 548
Joulain, K., Falgarone, E., Des Forets, G. P., & Flower, D. 1998, A&A, 340, 241
Jura, M. 1975, ApJ, 197, 581
Lacour, S., Ziskin, V., Hébrard, G., et al. 2005, ApJ, 627, 251
Le Petit, F., Nehmé, C., Le Bourlot, J., & Roueff, E. 2006, ApJS, 164, 506
Le Petit, F., Roueff, E., & Herbst, E. 2004, A&A, 417, 993
Ledoux, C., Petitjean, P., & Srianand, R. 2003, MNRAS, 346, 209
Ledoux, C., Petitjean, P., & Srianand, R. 2006, ApJ, 640, L25
Lehner, N., Wakker, B. P., & Savage, B. D. 2004, ApJ, 615, 767
Levshakov, S. A., Dessauges-Zavadsky, M., D'Odorico, S., & Molaro, P. 2002, ApJ, 565, 696
Lu, L., Sargent, W. L. W., Barlow, T. A., Churchill, C. W., & Vogt, S. S. 1996, ApJS, 107, 475
Mandy, M. E., & Martin, P. G. 1993, ApJS, 86, 199
Mathis, J. S., Rumpl, W., & Nordsieck, K. H. 1977, ApJ, 217, 425
Morton, D. C. 1991, ApJS, 77, 119
Morton, D. C. 2003, ApJS, 149, 205
Noterdaeme, P., Petitjean, P., Srianand, R., Ledoux, C., & Le Petit, F. 2007, A&A, 469, 425
Petitjean, P., Ledoux, C., Noterdaeme, P., & Srianand, R. 2006, A&A, 456, L9
Prochaska, J. X., & Wolfe, A. M. 2002, ApJ, 566, 68

Pottasch, S. R., Wesselius, P. R., & van Duinen, R. J. 1979, A&A, 74, L15
Prochaska, J. X., Herbert-Fort, S., & Wolfe, A. M. 2005, ApJ, 635, 123
Rachford, B. L., Snow, T. P., Tumlinson, J., et al. 2002, ApJ, 577, 221
Rodríguez, E., Petitjean, P., Aracil, B., Ledoux, C., & Srianand, R. 2006, A&A, 446, 791
Roy, N., Chengalur, J. N., & Srianand, R. 2006, MNRAS, 365, L1
Sargent, W. L. W., Boksenberg, A., & Steidel, C. C. 1988, ApJS, 68, 539
Savage, B. D., & Sembach, K. R. 1996, ApJ, 470, 893
Savage, B. D., Bohlin, R. C., Drake, J. F., & Budich, W. 1977, ApJ, 216, 291
Silva, A. I., & Viegas, S. M. 2001, Computer Phys. Commun., 136, 319
Smette, A., Wisotzki, L., Ledoux, C., et al. 2005, in Probing Galaxies through Quasar Absorption Lines, ed. P. Williams, C.-G. Shu, & B. Menard, IAU Colloq., 199, 475
Spitzer, Jr., L., & Jenkins, E. B. 1975, ARA&A, 13, 133
Spitzer, L. J., & Cochran, W. D. 1973, ApJ, 186, L23
Spitzer, Jr., L., Cochran, W. D., & Hirshfeld, A. 1974, ApJS, 28, 373
Srianand, R., Petitjean, P., Ledoux, C., Ferland, G., & Shaw, G. 2005, MNRAS, 362, 549
Weingartner, J. C., & Draine, B. T. 2001, ApJS, 134, 263
Welty, D. E., Frisch, P. C., Sonneborn, G., & York, D. G. 1999, ApJ, 512, 636
Welty, D. E., Lauroesch, J. T., Blades, J. C., Hobbs, L. M., & York, D. G. 2001, ApJ, 554, L75
Wolfe, A. M., Prochaska, J. X., & Gawiser, E. 2003, ApJ, 593, 215
Wolfe, A. M., Gawiser, E., & Prochaska, J. X. 2005, ARA&A, 43, 861

Online Material

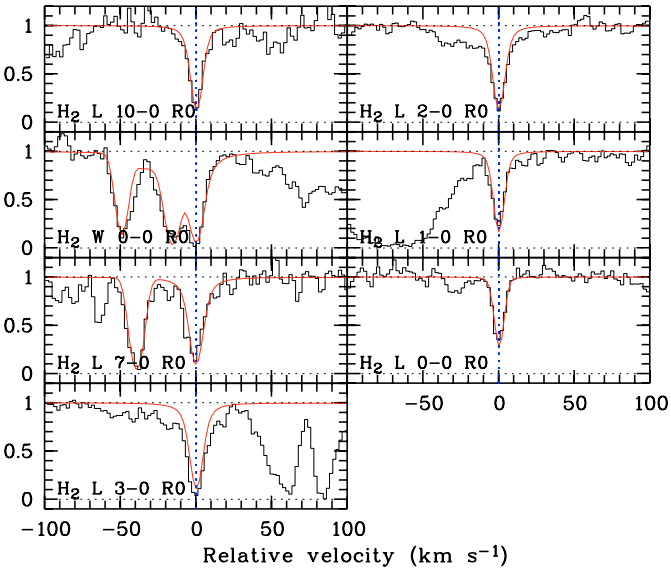

Fig. 19. Absorption lines from H_2 in rotational level $J = 0$ at $z_{abs} = 2.40183$ toward HE 0027−1836.

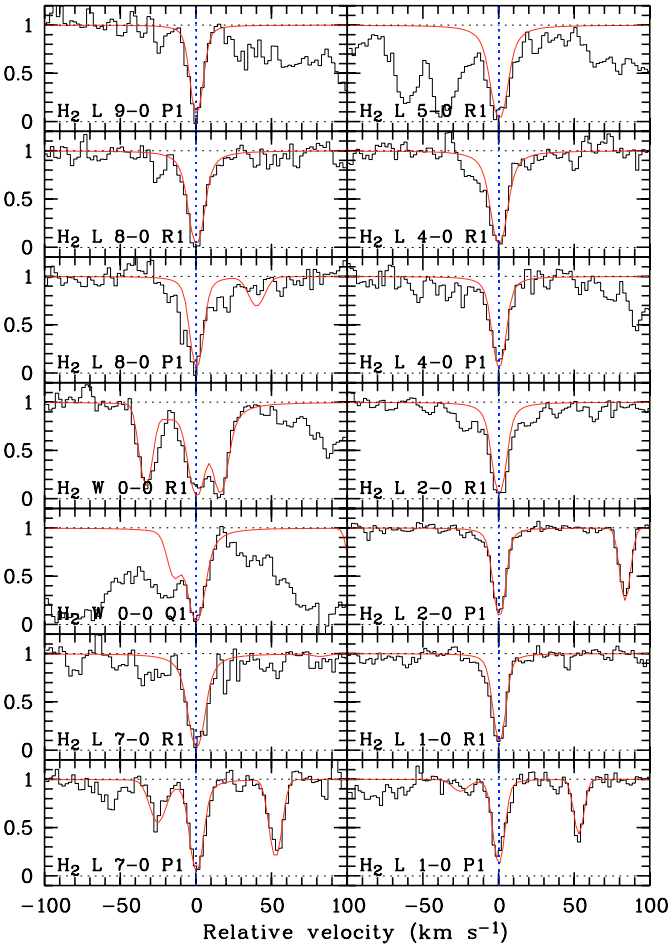

Fig. 20. Absorption lines from H_2 in rotational level $J = 1$ at $z_{abs} = 2.40183$ toward HE 0027−1836. One can see that damping wings are present for H_2 L8-0 R1.

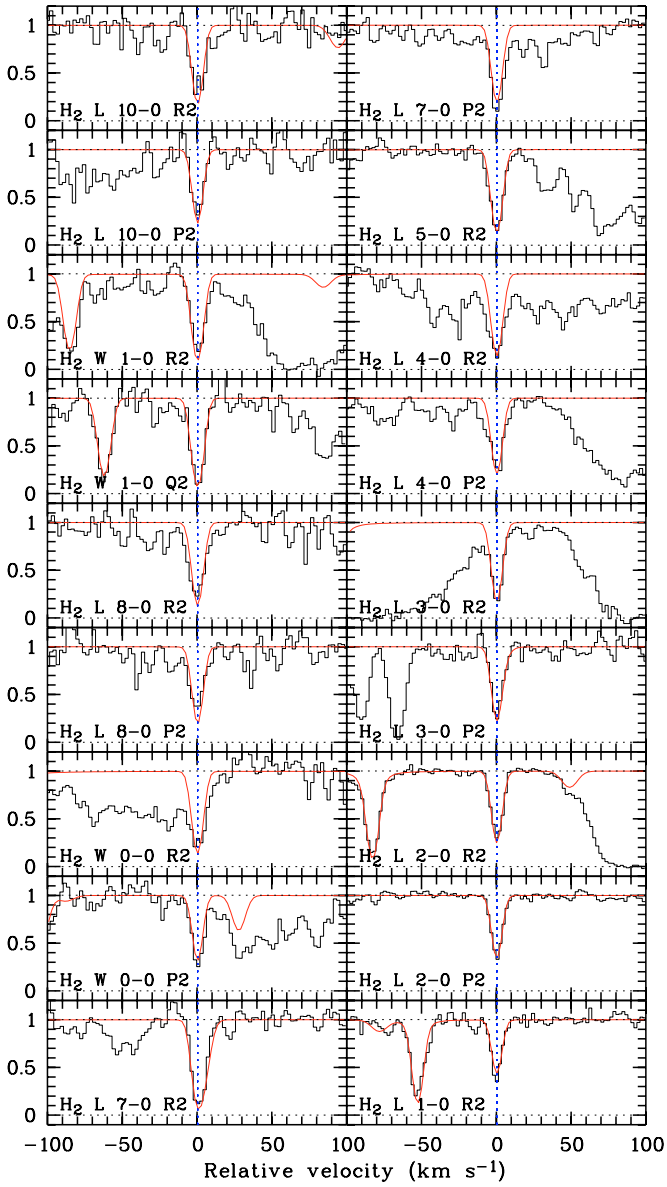

Fig. 21. Absorption lines from H_2 in rotational level $J = 2$ at $z_{abs} = 2.40183$ toward HE 0027−1836. Note the high signal-to-noise ratio in the H_2 L2-0 R2 and H_2 L2-0 P2 panels.

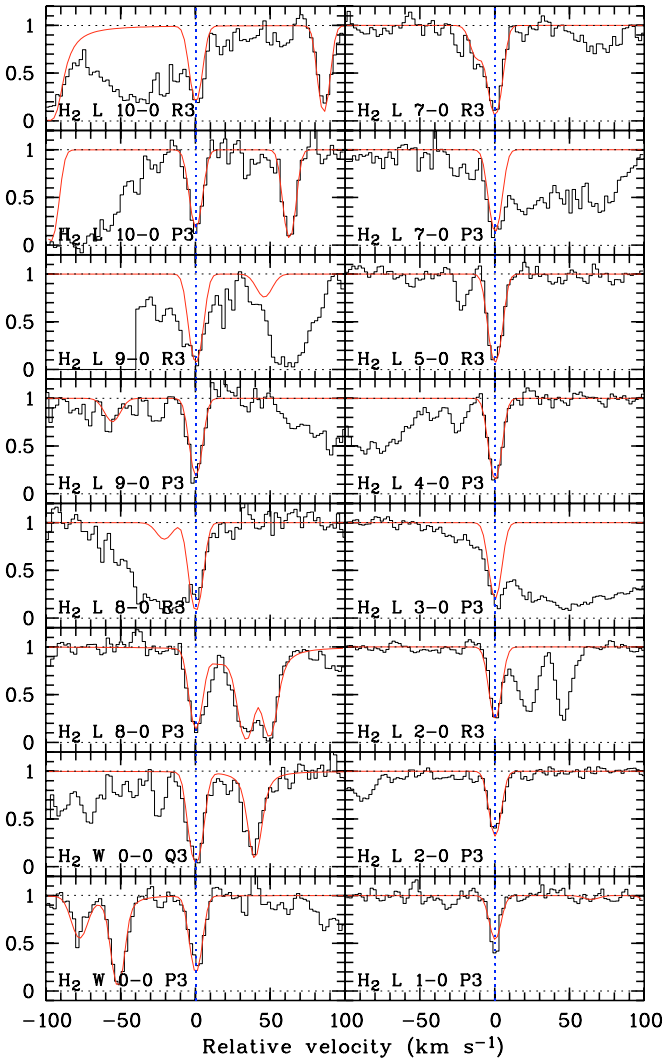

Fig. 22. Absorption lines from H_2 in rotational level $J = 3$ at $z_{abs} = 2.40183$ toward HE 0027−1836.

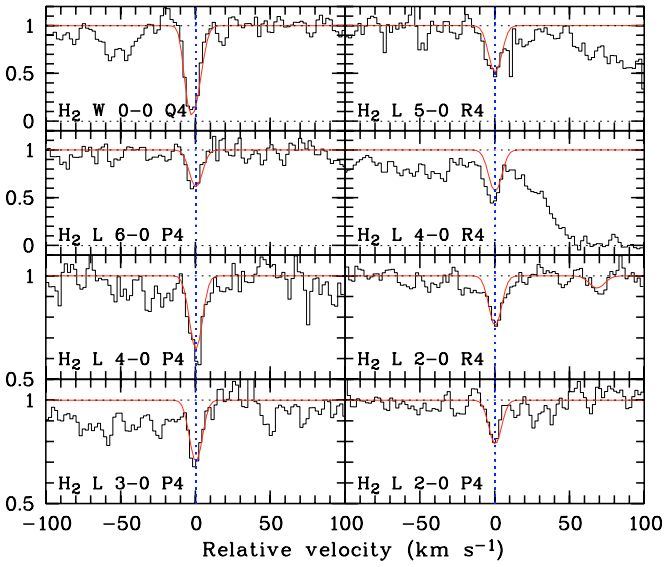

Fig. 23. Absorption lines from H_2 in rotational level $J = 4$ at $z_{abs} = 2.40183$ toward HE 0027−1836. The H_2 W0-0 Q4 transition is actually blended with H_2 L7-0 R2 which provides most of the absorption.

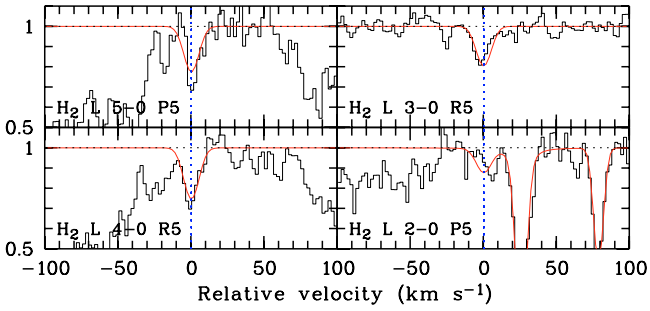

Fig. 24. Absorption lines from H_2 in rotational level $J = 5$ at $z_{abs} = 2.40183$ toward HE 0027−1836.

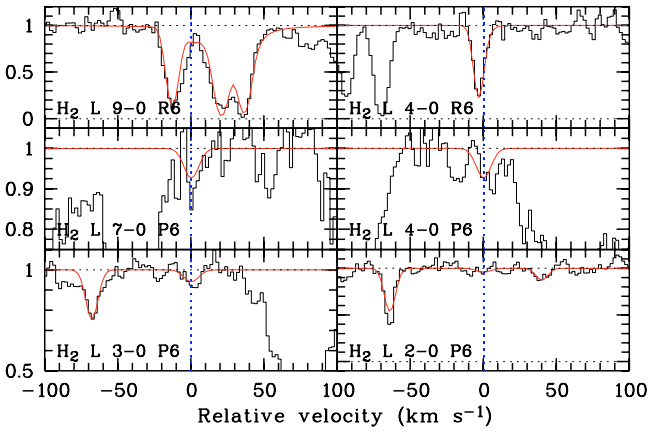

Fig. 25. Possible detection of H_2 in rotational level $J = 6$ at $z_{abs} = 2.40183$ toward HE 0027−1836. A consistent absorption feature is seen in the H_2 L3-0 P6 panel, and explains the slight asymmetry in the H_2 L4-0 R6 panel, which actually is a blend of H_2 L3-0 P2 together with H_2 L4-0 R6.